# A Probabilistic Method for Estimation of Bowel Wall Thickness in MR Colonography

Thomas Hampshire[1]*, Alex Menys[2], Asif Jaffer[2], Gauraang Bhatnagar[2], Shonit Punwani[2], David Atkinson[2], Steve Halligan[2], David J. Hawkes[1], Stuart A. Taylor[2]

1 Centre for Medical Image Computing (CMIC), University College London (UCL), Gower Street, London WC1E 6BT, United Kingdom, **2** Centre for Medical Imaging, University College London, 250 Euston Road, London NW1 2PG, United Kingdom

* thomas.hampshire.09@ucl.ac.uk
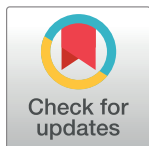
Abstract

MRI has recently been applied as a tool to quantitatively evaluate the response to therapy in patients with Crohn's disease, and is the preferred choice for repeated imaging. Bowel wall thickness on MRI is an important biomarker of underlying inflammatory activity, being abnormally increased in the acute phase and reducing in response to successful therapy; however, a poor level of interobserver agreement of measured thickness is reported and therefore a system for accurate, robust and reproducible measurements is desirable. We propose a novel method for estimating bowel wall-thickness to improve the poor interobserver agreement of the manual procedure. We show that the variability of wall thickness measurement between the algorithm and observer measurements ($0.25mm \pm 0.81mm$) has differences which are similar to observer variability ($0.16mm \pm 0.64mm$).

1 Introduction

1.1 Motivation

Crohn's disease (CD) is an important healthcare problem which affects 700,000 people in the USA and 500,000 in Europe [1, 2]. CD manifests as a relapsing inflammatory disease that mainly affects the gastro-intestinal tract, producing disabling symptoms including abdominal pain, diarrhoea and vomiting, weight loss, loss of appetite, arthralgias (joint paint), fever, and fatigue [3]. Management of CD is multi-disciplinary and revolves around immunosuppressive therapy and judicious use of surgical resection. The disease has a lifelong relapsing course with periods of acute inflammatory activity interspaced with periods of relative quiescence [1, 3]. The key to successful management is correct identification of the active phase such that appropriate treatment with immunosuppressive medication can be instigated and remission sustained. Such medications however attract a significant side effect profile and not all patients respond. Another important facet of disease management is therefore monitoring of therapeutic effect such that treatment regimens can be changed as appropriate. Identification of active disease and morning of therapeutic effect in CD is problematic [1]. Arguably the gold standard is endoscopy which can visualise the mucosa of the colon and terminal ileum. However the

test is highly invasive, expense, and cannot assess extra luminal complications or the proximal
small bowel. Blood and stool tests such as CRP and faecal calprotectin have a role but lack both
sensitivity and specificity. Cross sectional imaging, particularly MRI is increasing using to
diagnose relapse in CD and monitor therapeutic interventions [4]. In the case of MRI, the test
is non-invasive and does not impart ionising radiation. Furthermore it is able to assess both
luminal and extra luminal disease including abscess and fistulation [5]. Various parameters on
MRI have been validated as biomarkers of disease activity against both endoscopy and histopa-
thology. Notably bowel wall thickness, T2 weighted mural signal and contrast enhancement
on post gadolinium T1 weighted images are highly correlated with inflammatory activity [6,
7]. MRI activity scores have been derived which include these parameters. For example the
Magnetic Resonance Index of Activity (MaRIA) score is highly correlated with an endoscopic
activity score (Crohn's Disease Endoscopic Index of Activity) and includes evaluation of all
these MRI features as well as ulceration by the reporting radiologist [8]. Similarly, Steward
et all developed an MRI activity score using surgical resection specimens and subsequently val-
idated it against endoscopic biopsy [9]. Again the main facets of the scoring system are bowel
wall thickness, T2 mural signal and contrast enhancement. Importantly, this score has recently
been show to accurately reflect therapeutic response [10]. Such scoring systems require good
inter and intra observer variation. Furthermore they are time consuming to apply in clinical
practice. Measurement of bowel wall thickness is a vital part of activity scoring but is subject to
inter-observer variation and is particularly time consuming, requiring manual placement of
electronic callipers by the reporting radiologist. Automation of bowel wall thickness measure-
ment to improve accuracy and efficiency is therefore highly desirable.

1.2 Related Work - Technical

The need for a computer-assisted model for automated detection of mural inflammation in
patients with Crohn's disease was identified in [11]. The ability to grade disease severity is rec-
ognised as limited due to the weak to moderate interobserver variability of subjective MRI fea-
tures [12]. A pipeline for automated assessment of disease severity was introduced by [13],
including procedures for image analysis, classification and visualisation to predict colonoscopy
disease score. Included is a proposal of a bowel wall segmentation method to allow analysis of
bowel wall thickness as a function of time; a method for registration of Dynamic Contrast
Enhanced MRI (DCE-MRI) images, to allow for generation of accurate Time Injection Curves
(TIC); a method for identification of diseased regions by classification of texture features by
machine learning techniques; and finally a method for effective visualisation of disease by vol-
ume rendering.

In [14] low level features based on image intensity, texture and shape asymmetry are com-
bined with a supervised learning approach to classify patches of pixels in abdominal MRI
images as 'diseased' or 'normal'. Texture maps are created based on Gabor filter banks, and
shape asymmetry features based on entropy of orientation distributions with each patch pro-
viding multidimensional features. A range of classifiers are used: random forests, support vec-
tor machines, and a naive Bayesian classifier giving a high level of classification accuracy. [15]
extend this method to perform efficient classification over a large volume, by first segmenting
the volume into super voxels by a k-means clustering of voxels using image boundary informa-
tion [16]. This allows random forest classification of supervoxels followed by graph cut seg-
mentation to identify contiguous regions of disease. Most recently in [17], feature vectors are
extracted from overlapping 8×8 voxel image patches. A query sample selection helps select
the most informative unlabelled patches by visual saliency, allowing a radiologist to classify the

patches with the most contextual information. Again, graph-cuts are used to segment the volume based on the image patches to classify areas of disease.

[18] propose a method to perform non-rigid motion correction in free-breathing abdominal DCE-MRI data. A large number of volumes are dynamically acquired and retrospective gating used to select those volumes which are in a similar point in the respiratory cycles, based on the sum-of-squared-differences error between them. A Discrete Cosine Transformation (DCT) [19] is then used to co-register all selected volumes to a reference volume. The effectiveness of the algorithm is evaluated by assessment of the TICs in three regions of interest, showing less fluctuation in the gated and registered images, in comparison to the entire dynamic volume stack.

A method for measurement of wall thickness of the colon using ultrasound has been published [20]. Multiple methods are evaluated for segmentation of a single image slice: Otsu's thresholding [21], followed by region growing; level set segmentation; adaptive thresholding; Canny edge detection. The distance across these segmented region is measured and compared against a human reader. Results for a very small sample size (n = 5) are shown.

1.3 Proposed method

The following contributions are described in further detail in section 2:

- A novel method to automatically track sections of colon, and subsequently make measurements of thickness of circumferential loops of the bowel wall. A state distribution is used to model the bowel, with each state corresponding to a position, orientation and shape of the lumen. A Bayesian recursion equation is applied to estimate the posterior density of the state space, by repeating prediction and measurement steps based on the MRI volume, using a framework called particle filtering [22]. The resulting density is then used to calculate the centreline position. Although not applied to the bowel before, this framework has been used in the tracking of cerebral arterial segments [23].

- A novel method is proposed to estimate the positions of the inner and outer bowel wall by analysis of cross sections corresponding to the plane perpendicular to the centreline. The problem is modelled with a MRF, using gradient based metrics extracted from the MRI volume to assign costs to each possible bowel wall position. Performing inference on this model allows estimation of the optimal position of the inner and outer bowel wall, and therefore the thickness. This method is shown to give similar thickness measurements, and a similar level of inter-observer variability to the human reader.

2 Methods

2.1 Overview

As a first step, the bowel is tracked using the particle filter method described in section 2.2. The resulting particle information is used to extract a smooth centreline using the fast marching technique described in section 2.5.2. Finally, the positions of the inner and subsequently the outer bowel wall are computed using image gradient information and a MRF model using the method described in section 2.6. This overview is shown in Fig 1.

2.2 Particle Filter

The theory and algorithms in [22] can be used to estimate the state of a dynamic system given a sequence of noisy measurements. They are often used to measure the evolution of state over time, although any dynamic factor can be substituted. In the following section we propose to
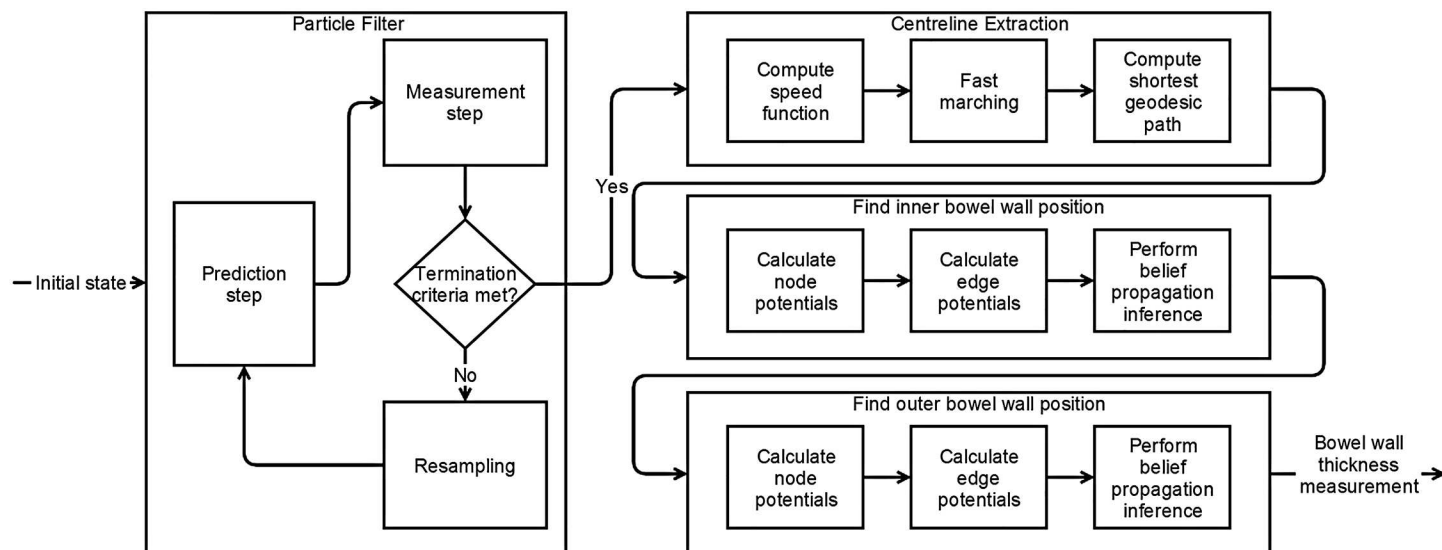
Fig 1. A flowchart providing an overview of the method to perform automated bowel wall thickness measurements.

doi:10.1371/journal.pone.0168317.g001

track the colon by evolving the state of a system containing the central position of the bowel as well as its orientation and cross sectional shape. Initially the shape will be modelled with an ellipse with varying radius and orientation. The assumption of smooth variation along the axis of the structure gives a good argument for the use of a tracking-based solution.

2.3 State Vector

The initial state of the system is modelled as a 15-D vector:

$$\mathbf{x}_t \quad = \quad [c_{x_t}\ c_{y_t}\ c_{z_t}\ r_{11_t}\ r_{12_t}\ r_{13_t}\ r_{21_t}\ r_{22_t}\ r_{23_t}\ r_{31_t}\ r_{32_t}\ r_{33_t}\ a_t\ b_t\ \phi_t]^T \tag{1}$$

$$= \quad [\mathbf{c}_t^T\ \mathbf{r}_t^T\ \mathbf{e}_t^T]^T, \tag{2}$$

where $\mathbf{c}_t$ represents the centre of the structure at time t, $\mathbf{r}_t$ represents the elements of a reference frame $\mathbf{R}_t$ given by:

$$\mathbf{R}_t = \begin{bmatrix} r_{11_t} & r_{12_t} & r_{13_t} \\ r_{21_t} & r_{22_t} & r_{23_t} \\ r_{31_t} & r_{32_t} & r_{33_t} \end{bmatrix}, \tag{3}$$

giving a global orientation, and $\mathbf{e}_t$ represents the ellipse parameters comprising the length of the ellipse major a_t and minor b_t axes, as well as the orientation ϕ_t relative to reference frame $\mathbf{R}$.

2.4 Prediction Model

The state prediction is modelled as an addition of the normal vector to the position vector with the addition of a zero mean Gaussian noise vector ϵ_c:

$$\mathbf{c}_t = \mathbf{c}_{t-1} + [r_{13_t}\ r_{23_t}\ r_{33_t}]^T + \epsilon_c. \tag{4}$$

Similarly, the ellipse parameters are corrupted by Gaussian noise vector ϵ_e:

$$\mathbf{e}_t = \mathbf{e}_{t-1} + \epsilon_e. \tag{5}$$

The reference frame is however perturbed by a function whose behaviour is defined in the following section:

$$\mathbf{R}_t = f_n(\mathbf{R}_{t-1}, \epsilon_r) \tag{6}$$

2.4.1 Normal Vector Perturbation. Without lack of generality, the mean orientation of the normal noise vector can be considered to be in the direction $(0, 0, 1)$. This can be represented in terms of spherical coordinates, with a polar angle ϵ_θ and azimuth ϵ_ψ as:

$$\epsilon_r = [\cos\epsilon_\theta \sin\epsilon_\psi \quad \sin\epsilon_\theta \sin\epsilon_\psi \quad \cos\epsilon_\psi]^T. \tag{7}$$

ϵ_θ can be sampled from the uniform distribution (displayed in Fig 2):

$$\epsilon_\theta \sim \mathcal{U}(0, 2\pi), \tag{8}$$

and ϵ_ψ is normally distributed around 0, such that the samples are more sparse the further the angle from the pole:

$$\epsilon_\psi \sim \mathcal{N}(0, \sigma_\psi^2). \tag{9}$$

With the assumption that the particle position $\mathbf{c}'_{t-1} = [0\ 0\ 1]^T$ and $\mathbf{c}'_t = [cos\epsilon_\theta \quad sin\epsilon_\psi \quad sin\epsilon_\theta\ sin\epsilon_\psi \quad cos\epsilon_\psi]^T$ and rotation frames:

$$\mathbf{R}'_{t-1} = \begin{bmatrix} 1 & 0 & 0 \\ 0 & 1 & 0 \\ 0 & 0 & 1 \end{bmatrix}, \quad \mathbf{R}'_t = \begin{bmatrix} \phi_a & \phi_b & \cos\epsilon_\theta\ \sin\epsilon_\psi \\ \phi_c & \phi_d & \sin\epsilon_\theta\ \sin\epsilon_\psi \\ \phi_e & \phi_f & \cos\epsilon_\psi \end{bmatrix}, \tag{10}$$

the variables $\phi_a, \ldots, \phi_f$ of reference frame $\mathbf{R}'_t$ that minimise the twist between frame $\mathbf{R}'_{t-1}$ and $\mathbf{R}'_t$ can be found by sweeping a Rotation Minimizing Frame (RMF) through points $\mathbf{c}'_{t-1}$ and $\mathbf{c}'_t$ using the double reflection method in [24]. This 'local' reference frame $\mathbf{R}'_t$ can be used to update the global reference frame $\mathbf{R}_t$ in the state vector using:

$$\mathbf{R}_t = \mathbf{R}_{t-1}\mathbf{R}'_t. \tag{11}$$

2.5 Measurement Model

The proposed model uses cross-sectional radial intensity profiles to assign a probability of the observed data $\mathbf{z}_t$ given a state $\mathbf{x}_t$. We use the approximation that the colon is topologically cylindrical, with an elliptical cross-section of varying parameters (see Fig 3). The assumption is made that the intra-luminal space has a low local intensity, relative to the bowel wall, due to the ingested contrast agent. At the position of the colon wall, a rapid increase in the image intensity is observed. It is this increase in image intensity that is detected across the radial intensity profile by defining an intensity threshold. The likelihood function $p(\mathbf{z}_t|\mathbf{x}_t)$ is then defined using the proximity of the detected boundary points to the predicted ellipse. The
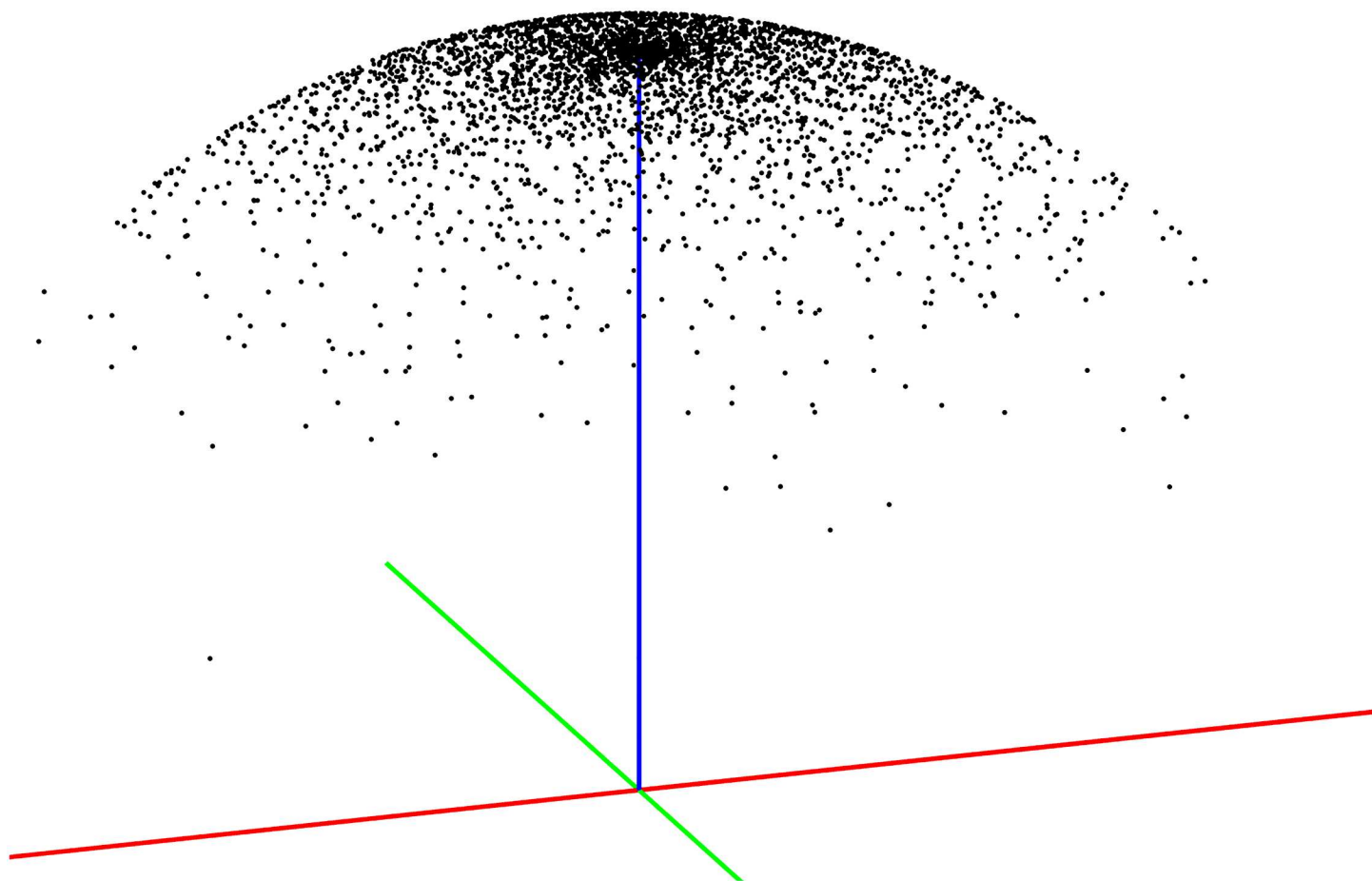
Fig 2. Perturbation of the state normal vector from a uniform azimuth and normally distributed polar angle. Here, a set of example samples are displayed as black markers, about the previous normal vector displayed in blue.

ellipse boundary positions $\mathbf{u}$ are defined as:

$$\mathbf{u}_t^h = \mathbf{R}_t \begin{bmatrix} a_t\cos(h)\cos(\phi_t) - b_t\sin(h)\sin(\phi) \\ a_t\cos(h)\sin(\phi_t) + b_t\sin(h)\cos(\phi) \\ 0 \end{bmatrix} + \mathbf{c}_t, \qquad (12)$$

where $h \sim [0, 2\pi]$ and H is the number of sampled positions. Similarly, the unit vector from $\mathbf{c}_t$ to each point in $\mathbf{u}$ is used to interpolate a radial intensity profile and detect the bowel wall given by an intensity value exceeding some threshold k. A term is included to penalise states in which bowel wall is detected within an inner ellipse defined by:

$$\mathbf{u}_{inner_t}^h = \mathbf{R}_t \left(\eta \begin{bmatrix} a_t\cos(h)\cos(\phi_t) - b_t\sin(h)\sin(\phi) \\ a_t\cos(h)\sin(\phi_t) + b_t\sin(h)\cos(\phi) \\ 0 \end{bmatrix} \right) + \mathbf{c}_t, \qquad (13)$$
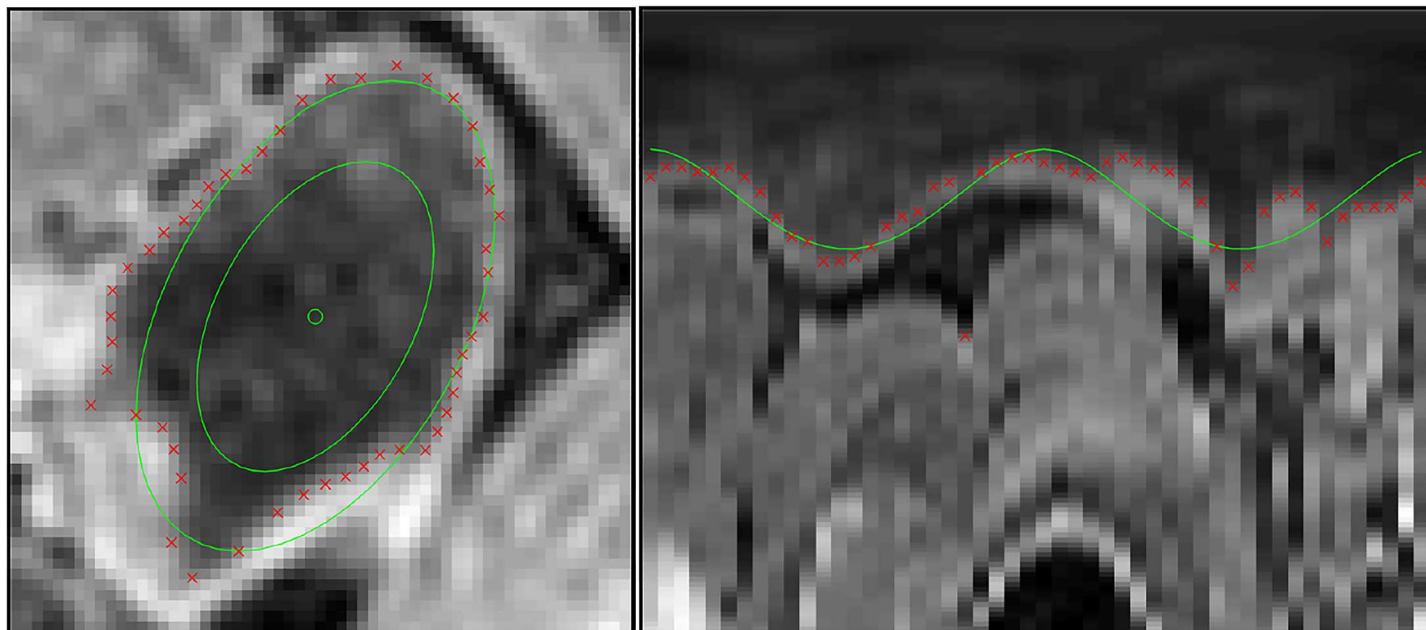
Fig 3. Measurement of a single state visualised in both crosssection view (left) and radial coordinates (right). Ellipse parameters are visualised in green, and detected colon wall points are marked in red.

doi:10.1371/journal.pone.0168317.g003

designed to further discourage crossing of the bowel wall. Lastly, some boundary points may not be detected, and so these are excluded from the measurement model calculation, but incur an additional penalty based on the percentage of missing boundary points. A cost function is then defined as the mean sum of squared distances between the detected boundary points $\mathbf{v}$ and the ellipse $\mathbf{u}$:

$$F_{v,u}(\mathbf{v}_t^{h^i}, \mathbf{u}_t^{h^i}) = \frac{\sum_{h=0}^{2\pi} ||\mathbf{v}_t^{h^i} - \mathbf{u}_t^{h^i}||}{H_{detected}}. \tag{14}$$

where $H_{detected}$ is the number of detected boundary points. The full measurement model is then:

$$d(\mathbf{z}_t|\mathbf{x}_t^i) = \frac{F_{v,u}(\mathbf{v}_t^{h^i}, \mathbf{u}_t^{h^i})}{(1 - \Upsilon)\Omega}, \tag{15}$$

where Υ is the percentage of boundary points detected within inner ellipse $\mathbf{u}_{inner_t}^h$, and Ω is the proportion of detected boundary points. The particle weights can be calculated:

$$q_k^i \propto q_{k-1}^i \frac{\exp(-Wd(\mathbf{z}_t|\mathbf{x}_t^i))}{\sum_{m=1}^{N_s} \exp(-Wd(\mathbf{z}_t|\mathbf{x}_t^m))}, \tag{16}$$

where W is a normalising constant and controls the sharpness of the weighting distribution.

The particle filter can be set to run to a maximum number of iterations T, or another termination criterion set such that a high rate of particle degeneracy is detected [25]. Here, a small effective sample size $\widehat{N_{eff}}$ indicates a high variance in the particle weights $\mathbf{q}^i$ and in turn indicates an unlikely state to represent the tracked bowel. This usually occurs due to local colonic

collapse, large amounts of high intensity intra-luminal matter, or poor image quality due to image artefact or poor bowel preparation. For this study, termination occurs when $\widehat{N_{eff}}$ is less than 1% of the original particle count.

2.5.1 Dynamic bowel wall intensity threshold. For robust tracking of the bowel wall, the wall intensity threshold k must be dynamically updated due to the local intensity inhomogeneity caused by the MRI bias field, and also the wall intensity inhomogeneity due to variations in contrast uptake. After each iteration t of the particle filter, voxel intensity values are sampled from the position of each detected inner wall position $\mathbf{P}$, along the vector which intersects this position and the position of the centreline $\mathbf{C_t}$. The voxel intensity values are split into two groups, the wall voxels $\mathbf{V^w}$ which start at wall position $\mathbf{P}$ and follow vector $\vec{\mathbf{C_t P}}$; and the lumen voxels $\mathbf{V^l}$ which follow vector $\vec{\mathbf{PC_t}}$. The distance sampled along each vector is set at $3mm$ as an approximate bowel wall thickness. Threshold k is found by linear search, such that it maximises the separation between these two groups:

$$k = \arg\max_k \left[\tau \sum_{i \in \mathbf{V^w}} f_>(V_i^w, k) + (1 - \tau) \sum_{i \in \mathbf{V^l}} f_<(V_i^l, k) \right], \tag{17}$$

where

$$f_>(x, k) = \begin{cases} 1 & \text{if } x > k \\ 0 & \text{otherwise} \end{cases}, \tag{18}$$

and

$$f_<(x, k) = \begin{cases} 1 & \text{if } x < k \\ 0 & \text{otherwise} \end{cases}. \tag{19}$$

2.5.2 Extraction of centreline. After the termination of the particle filter, a centreline is extracted to allow for subsequent measurement of the bowel wall thickness. A simple averaging of the particle centreline position at each iteration $\mathbf{C_t}$ gives unsatisfactory results in circumstances where the particle filter explores multiple pathways, as a mean position may not necessarily lie within the colon lumen. Instead, a speed function is derived from the particle positions at every iteration, and fast marching used to find the fastest geodesic path from start to end point. Speed function G can be created by computing the weighted sum of Gaussians:

$$G(y_j) = \sum_{i=1}^{N} q_i e^{||y_j - x_i||^2 / h^2} \tag{20}$$

where $\{x_i\}_{i=1,\dots,N}$ are the centres of the Gaussians, taken from the centreline positions of each particle state over all iterations; q_i are the weight coefficients taking from the respective particle weights; and h is the bandwidth parameter of the Gaussians (set experimentally to $3mm$). The sum of Gaussians is evaluated at each of the target points $\{y_j\}_{j=1,\dots,M}$, in this case the voxel coordinates of the input image domain in $\mathbb{R}^3$. This can be computed efficiently using a fast Gauss transform function [26]. The centreline can then be extracted by evolving a wave front across the image domain using the fast marching method [27], solving the Eikonal equation:

$$G(x)|\nabla T(x)| = 1, \tag{21}$$

where T is time. Centreline path is then found by computing the shortest geodesic distance
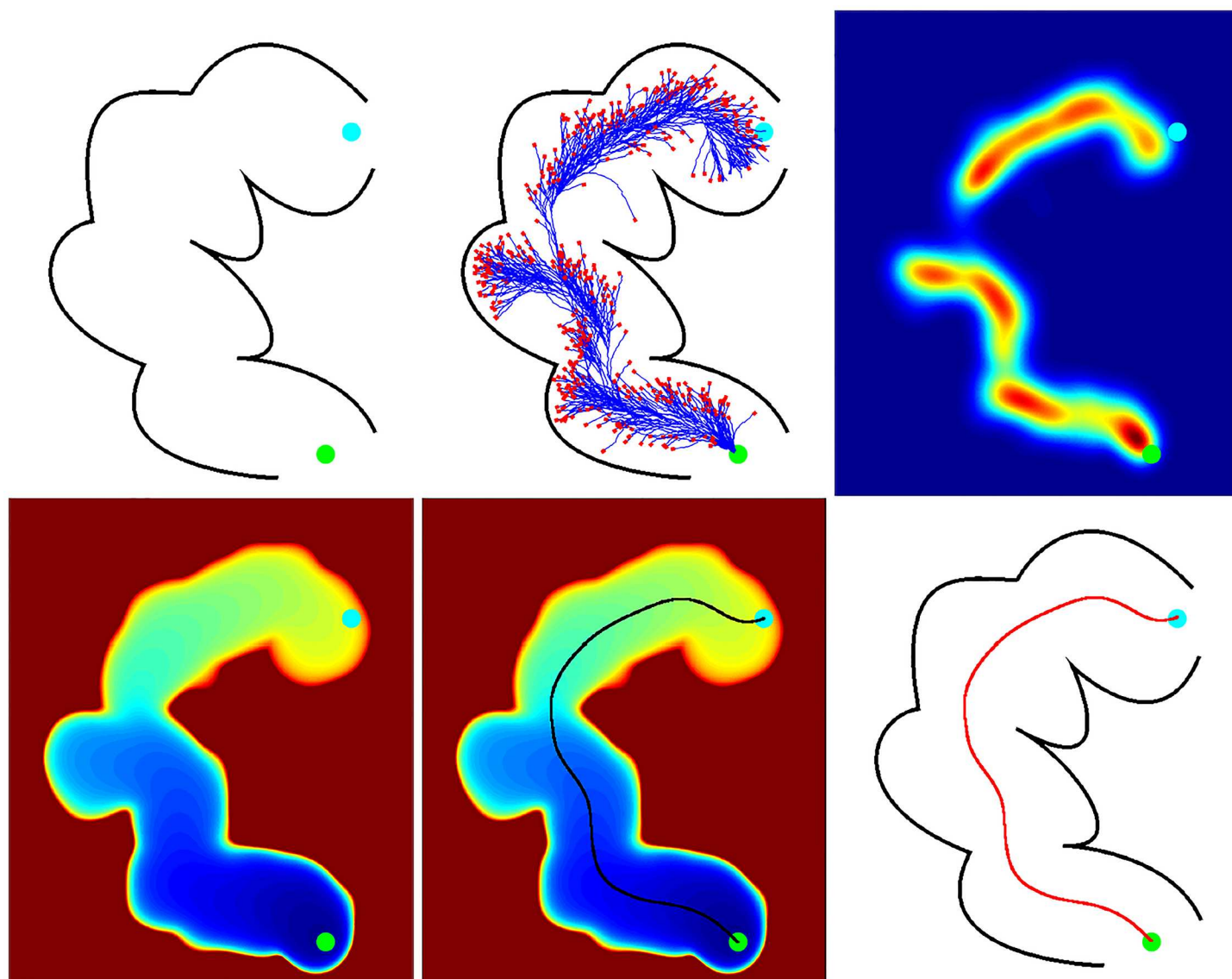
Fig 4. An overview of the particle filtering method. Top row shows: a segment of colon with particle filter start and end points in green and cyan respectively (left); execution of a simplified version of the particle filtering method showing 'live' and 'terminated' particles in blue and red respectively (middle); the speed function calculated from the weighted sum of Gaussians of particle positions (right). Bottom row shows: the geodesic distances from the start point, calculated by fast marching (left); the centreline path found by computing the shortest geodesic distance from start to end point (middle); the centreline path overlay on the original image (right).

doi:10.1371/journal.pone.0168317.g004

across the resulting distance map from start to end point. A simplified simulation of this workflow is demonstrated in Fig 4 and an example result displayed in Fig 5.

2.6 Wall thickness calculation

This section will describe the algorithm used to calculate the bowel wall thickness given a centreline path. To allow for a reference frame to be constructed at each position along the centreline **C**, a Rotation Minimising Frame (RMF) [28] is employed. The properties of such a set of reference frames are such that the magnitude of angles between the reference vectors of
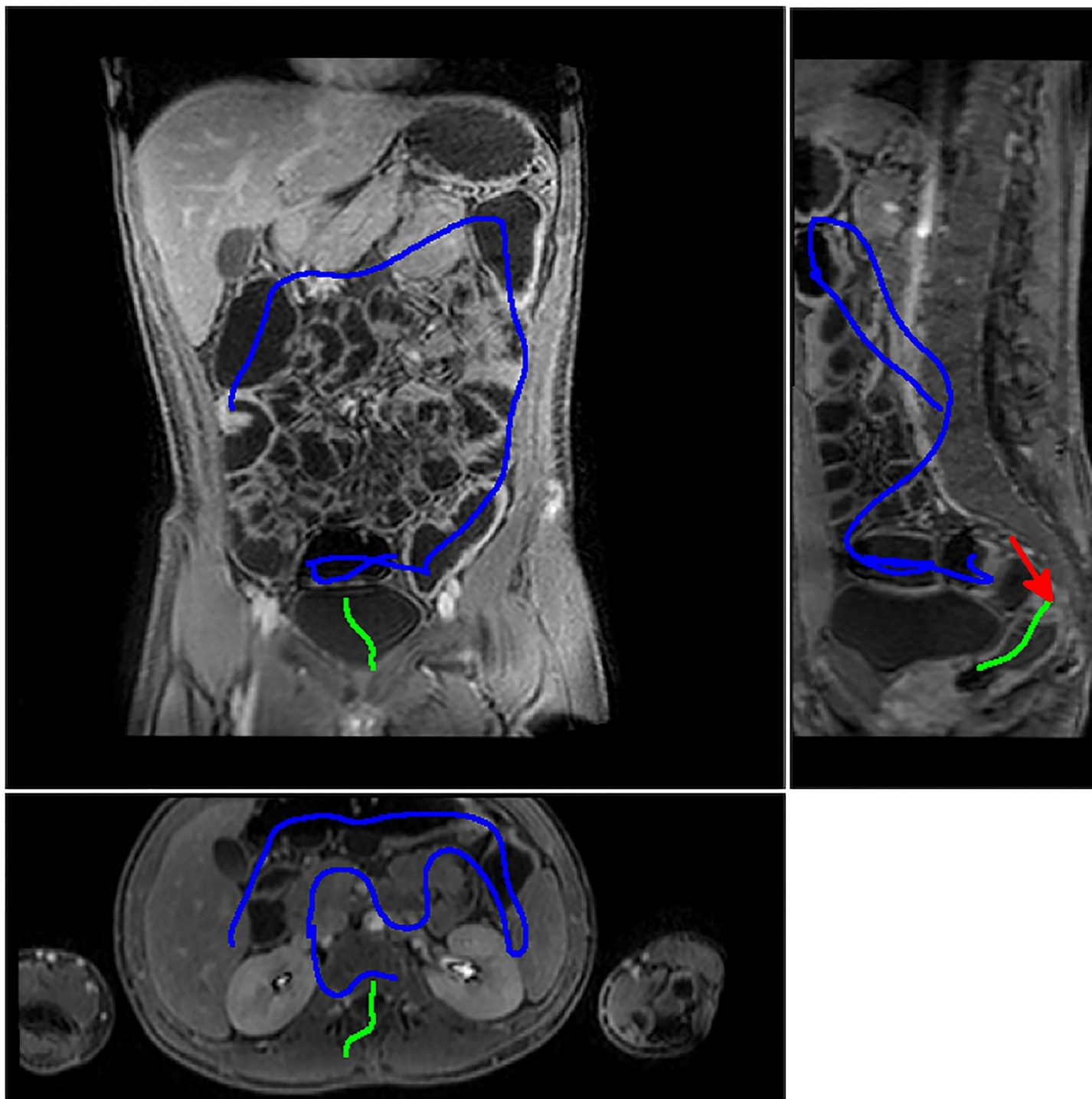
Fig 5. Particle filtering method applied to a patient dataset. The particle filter is first manually initialised in the rectum and tracks the colon to the sigmoid junction (green line) where it is unable to progress due to an area of local colonic collapse (indicated by the red arrow). The algorithm is manually reinitialised at the other side of the collapse and is able to track the colon through to the caecum (blue line). The figure shows both of these three dimensional lines projected onto a single coronal (top left), sagittal (top right) and axial (bottom) plane, and therefore travels in, and out of plane.

consecutive frames $U_i \, U_{i+1}$ are minimised, minimising the total global error:

$$E_g = \sum_{i=0}^{n-1} |\angle(U_i, U_{i+1})|. \tag{22}$$

Each frame can be defined by its components:

$$U = [\mathbf{r} \quad \mathbf{s} \quad \mathbf{t}], \tag{23}$$

where $\mathbf{t}$ defines the tangent vector, and $\mathbf{r}$ and $\mathbf{s}$ span the curve normal plane.

Now for any position along the centreline, it is assumed that there exists a full circumferential loop of bowel wall that lies in the image plane in which $\mathbf{r}$ and $\mathbf{s}$ lie. To more easily specify a point in this plane, a radial coordinate system is used, parametrised by θ, the angle of rotation from $\mathbf{r}$; and f, the distance from $\mathbf{C}$. As the bowel wall is a continuous structure, for each angle of rotation θ there exists a position of the inner bowel wall and so the task can be formulated as a labelling problem.

For every frame U_t there exists a set of sites $\mathbf{S}_t = \{1_t, \ldots, n_t\}$ which correspond to the angle of rotation around the frame tangent. A set of random variables $\mathbf{F}_t = \{F_{1_t}, \ldots, F_{n_t}\}$ which take a label corresponding to a distance from the frame centre $\mathbf{f}_t = \{f_{1_t}, \ldots, f_{n_t}\}$. A neighbourhood system defines edges and allow the definition of connections between sites $\mathbf{N}_t = \{N_{i_t} | \forall i_t \in \mathbf{S}_t\}$. Lastly a pairwise clique allows the modelling of the geometric and appearance based dependences between label configurations $\mathbf{C_2} = \{\{i_t, i'_t\} | i_t \in \mathbf{S}_t, i'_t \in N_{i_t}\}$.

Two types of edges are included within the model. The first allows inclusion of dependencies between neighbouring sites within the same frame and also between neighbouring frames $N_{i_t} = \{(i-1)_t, (i+1)_t, i_{t-1}, i_{t+1}\}$ (see Fig 6 for details).

2.6.1 Node Potentials - Inner Bowel Wall. The node potentials (see Fig 7) give a probability of assigning a label f_i to a site i. At the position of the inner bowel wall p_i at site i, a rapid change of the intensity of the image is expected, and the direction of this gradient should coincide with the unit vector $\hat{\mathbf{C}p_i} = \vec{\mathbf{C}p_i}/|\mathbf{C}p_i|$ from the frame centre to the site position. The following potentials are defined:

$$H_i^1(i) = \begin{cases} |\nabla I(p_i)| & \text{if } \nabla \hat{I}(p_i) \cdot \hat{\mathbf{C}p_i} > 0 \\ |\nabla I(p_i)|(\nabla \hat{I}(p_i) \cdot \hat{\mathbf{C}p_i} + 1)^2 & \text{otherwise} \end{cases} \tag{24}$$

This function penalises against selecting inner wall positions which have a gradient direction greater than $\pm\pi/4$ radians away from $\hat{\mathbf{C}p_i}$. Simply using the image gradient may produce some undesirable results when high contrast artefacts lie outside of the bowel wall, such as blood vessels or when two bowel walls are closely applied to each other. To prevent this from occurring, the result is scaled by the cumulative sum of voxel values from image I which lie above threshold k (the threshold which maximises the separation between the wall, and lumen voxels—see section 2.5.1), originating from the frame centre $\mathbf{C}$ along vector $\hat{\mathbf{C}p_i}$:

$$H_i^2(i) = \frac{\beta}{\sum_{n=0}^{f_i} f_>(I(\mathbf{C} + n\, \hat{\mathbf{C}p_i}), k)}, \tag{25}$$

where

$$f_>(x, k) = \begin{cases} 1 & \text{if } x > k \\ 0 & \text{otherwise} \end{cases}. \tag{26}$$
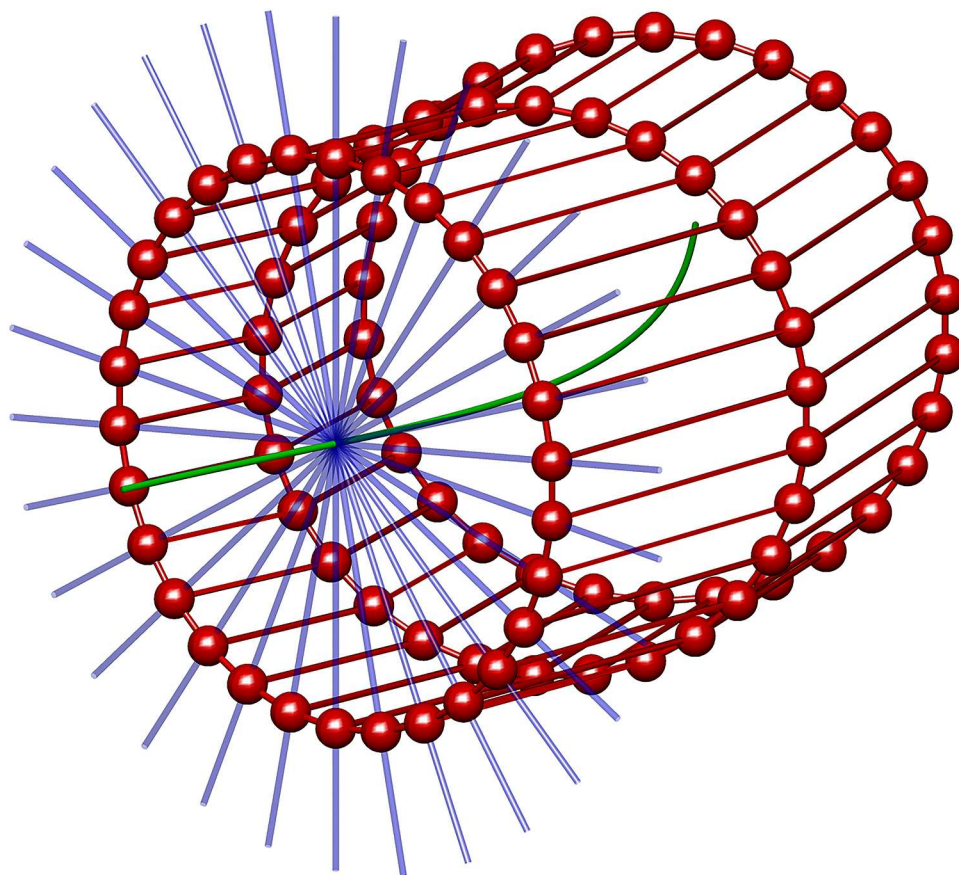
Fig 6. A simplified example of the graph structure described in section 2.6. At regular intervals along the centreline (green), a reference frame is extracted. In the image plane defined by this reference frame, a set of possible site locations are calculated by a radial coordinate system (blue). The set of sites corresponding to each reference frame may lie at any point along this ray. Here, for simplicity, the set of possible site locations for single a frame are shown, although the algorithm optimises over multiple frames. The sites are displayed as red spheres, connected by edges which describe their neighbourhood system. Neighbouring sets of rings correspond to neighbouring reference frames.

doi:10.1371/journal.pone.0168317.g006

and so the full site potential equation is:

$$V_i(i) = H_i^1(i)H_i^2(i). \tag{27}$$

2.6.2 Edge potentials - Inner Bowel Wall. The solution is constrained such that neighbouring sites must be both a similar distance to the centre of the frame, and have a similar voxel intensity value. This gives a result that is both continuous in terms of the bowel wall position, and the intensity of the signal at those positions. To model this, the following edge potentials are used:

$$V_{i,j}(i,j) = e^{-\gamma\|f_i - f_j\|}\left(1 - \frac{\min\left(I(p_i), I(p_j)\right)}{\max(I(p_i), I(p_j))}\right)^2, \tag{28}$$

where f_i is the distance of site i from the frame centre.
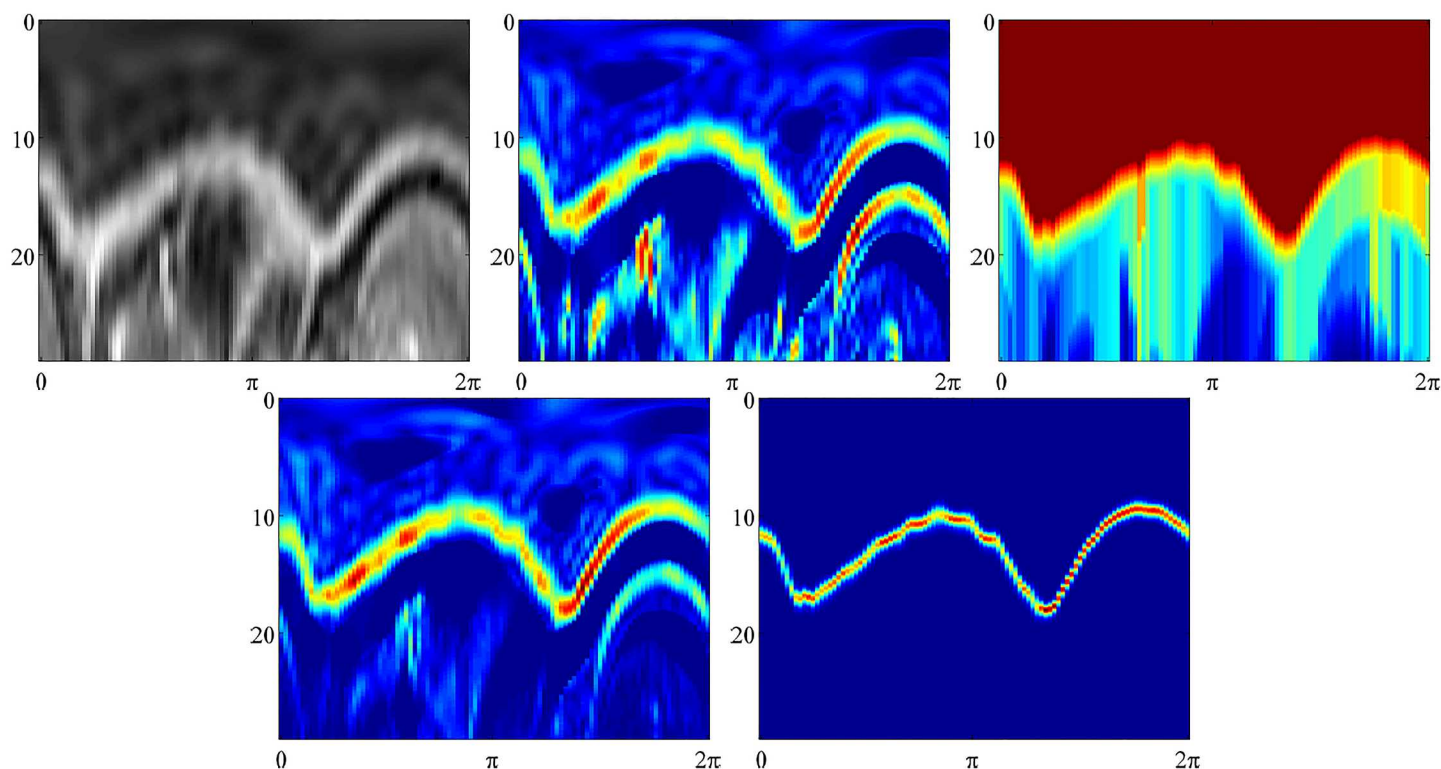
Fig 7. Figures show the construction of node potentials for the detection of the inner bowel wall. All figures are displayed in radial coordinates, with the distance from origin shown in the vertical axis, and the angle of rotation in the horizontal axis. The original image is shown top left. Top middle shows the gradient node potentials H_i^1. Top right shows the cumulative node potentials H_i^2. Bottom left shows the combined node potentials V_i. Bottom right shows the belief vectors b_j. All measures are scale invariant.

doi:10.1371/journal.pone.0168317.g007

2.6.3 Belief Propagation Inference. We wish to find the most probable solution of label assignments.

$$Pr(\mathbf{f}) = \frac{1}{Z} \prod_{i \in S} V_i(f_i) \prod_{i \in S} \prod_{j \in N_i} V_{ij}(f_i, f_j), \tag{29}$$

Z is intractable, but we can use the Max-product Belief Propagation (BP) algorithm to find the optimal global solution [29]:

$$\mathbf{f}^{(MAP)} = \arg\max_{\mathbf{f}} \left[\prod_{i \in S} V_i(f_i) \prod_{i \in S} \prod_{j \in N_i} V_{ij}(f_i, f_j) \right], \tag{30}$$

It is known that BP is exact on acyclic tree-like graphical models, but has been shown to give a good MAP estimate in graphs with loops. The BP algorithm works by passing messages between nodes of a graph defined by the set of sites $\boldsymbol{\theta}$, with edges defined by the site neighbourhoods $\mathbf{N}$. Each message M is an i dimensional vector, with i equal to the number of possible labels. At each iteration at time t, every node sends messages to each of its neighbours in parallel, whilst also receiving messages itself. Let $m_{p \to q}^t$ be the message that node p passes to node q at iteration t. All entries in $m_p^0 \to q$ are initialised to zero. At each iteration, new messages are

computed as follows:

$$m_{i \to j}^t(f_j) = \max_{f_i}\left(V_i(f_i)V_{ij}(f_i,f_j)\prod_{s \in N_i \backslash j} m_{s \to i}^{t-1}(f_i) \right),$$ (31)

where $N_i \backslash j$ denotes all neighbours of i other than j. After T iterations, the belief vector for each node may be computed:

$$b_j(f_j) = \left[V_j(f_j)\prod_{s \in N_j} m_{s \to j}^T(f_j) \right].$$ (32)

The belief vector $b_j(f_j)$ expresses the relative probability of assigning each label f_j to site j. Once the algorithm has terminated, each node is assigned the label having the maximum belief:

$$f_q^* = \arg\max_{f_q \in \mathbf{f}} b_q(f_q).$$ (33)

2.7 Calculation of the outer wall position

Following the completion of the BP algorithm, the MAP solution for the set of sites can be used to create a contour marking the position of the inner bowel wall. It can be assumed that there are a set of positions that lie along the normal vectors of this contour, that will also form a closed contour that coincides with the position of the outer bowel wall. Therefore, a similar protocol as described in the previous section can be followed, with the primary change being that the outer bowel wall positions are to be located relative to the inner bowel wall positions. However there are also changes made to the cost functions used.

2.7.1 Node potentials - Outer Bowel Wall.   Here, a solution with a rapid decrease in gradient in the direction of the normal of the inner bowel wall contour is desired (see Fig 8). A similar strategy as in Eq (24) is followed. This node potential differs only by the sign in the parentheses in comparison to the inner bowel wall node potential, which takes into account the direction of the gradient:

$$H_i^1(i) = \begin{cases} |\nabla I(p_i)| & \text{if } \nabla \hat{I}(p_i) \cdot \hat{\mathbf{C}p_i} < 0 \\ |\nabla I(p_i)|(\nabla \hat{I}(p_i) \cdot \hat{\mathbf{C}p_i} - 1)^2 & \text{otherwise} \end{cases}.$$ (34)

Similarly to the node potentials for the inner bowel wall, we wish to prevent a high potential value being assigned to high contrast artefacts which lie outside the bowel wall. For each site i, the position g_i of the first local minima in image gradient can be found along the vector from the frame centre to site $\hat{\mathbf{C}}_{p_i}$.

$$H_i^2(i) = \frac{\kappa}{F(p_i)},$$ (35)

where

$$F(p_i) = \begin{cases} 1 & \text{if } p_i = g_i \\ F(p_{i-1}) + 1 & \text{if } F(p_{i-1}) > 0 \\ 0 & \text{otherwise} \end{cases}$$ (36)
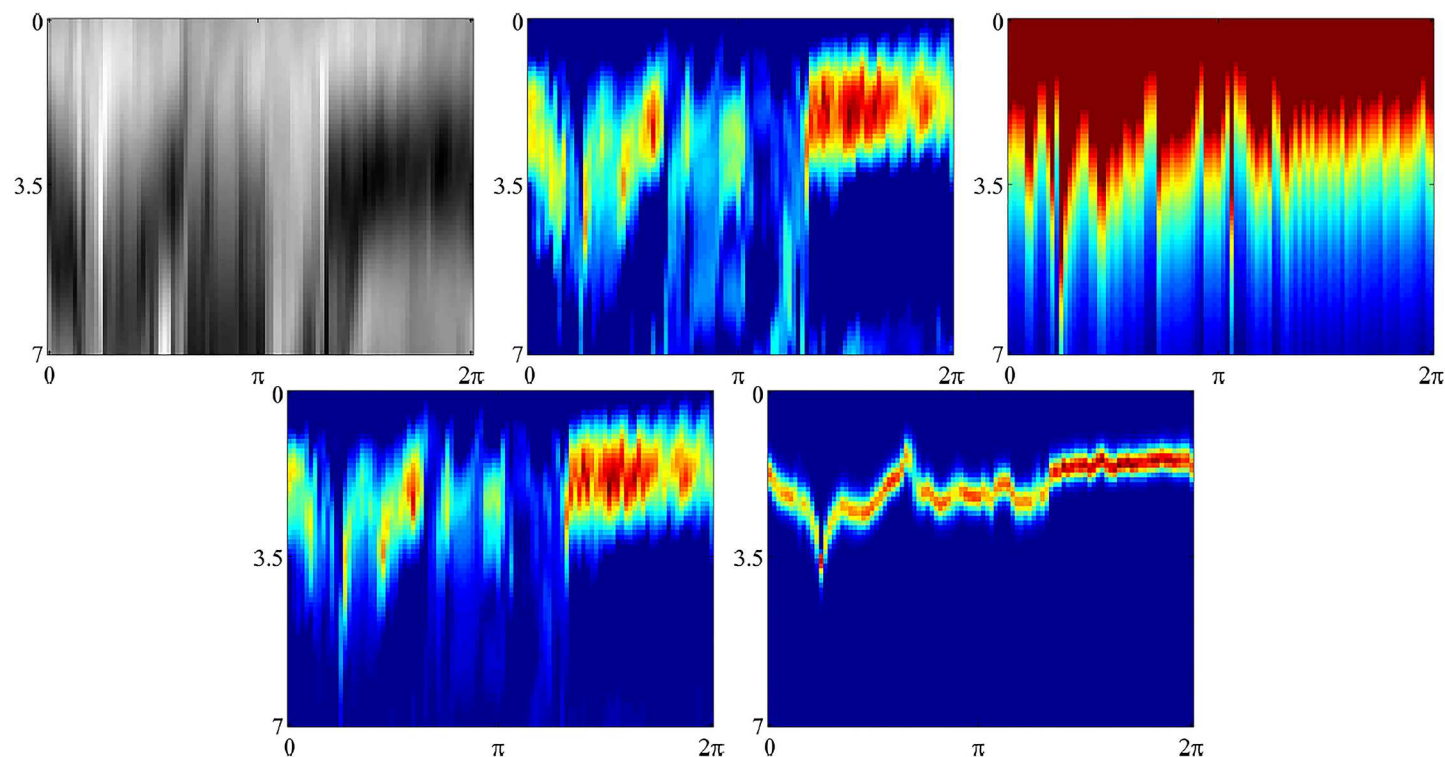
Fig 8. Figures show the construction of node potentials for the detection of the outer bowel wall. All figures are displayed in radial coordinates, with the distance from origin shown in the vertical axis, and the angle of rotation in the horizontal axis. The original image is shown top left. Top middle shows the gradient node potentials H_i^1. Top right shows the cumulative node potentials H_i^2. Bottom left shows the combined node potentials V_i. Bottom right shows the belief vectors b_j. All measures are scale invariant.

doi:10.1371/journal.pone.0168317.g008

2.7.2 Edge potentials - Outer Bowel Wall. Similar pair-wise constraints are applied to the outer as to the inner bowel wall for neighbouring sites. The solution is constrained so that the sites are a similar distance from the contour that defines the inner bowel wall, and the intensity of the signal at those positions must be similar. The same potentials as in Eq (28) are used. The label assignments are found using belief propagation. An example result for the wall thickness measurement is shown in Fig 9.

2.8 Algorithm Initialisation

The particle filter is initialised by setting all particles with the same parameters, therefore an initial state must be defined (see Eq (2)). The centre point parameters $[c_{x_1} \, c_{y_1} \, c_{z_1}]^T$ are selected with the use of a DICOM viewer to give a position in Euclidean space. The reference frame $\mathbf{R_1}$ is set such that the tangent $[r_{13_1} \, r_{23_1} \, r_{33_1}]^T$ is oriented along the colon lumen, and the other two frame vectors are set at arbitrary, orthogonal angles in the normal plane. The ellipse parameters $[a_1 \, b_1 \, \phi_1]^T$ are set by a semiautomatic method. First the volume is sampled along the intersecting plane defined by the normal vectors of R_1, to create the resliced image I_r spanning the normal plane. A graphical user interface (GUI) (see Fig 10) allows selection of points $z = [x \, y]$ in $\mathbb{R}^2$ defined by $\mathbf{R_1}$. An ellipse may be fit by least-squares minimisation [30].
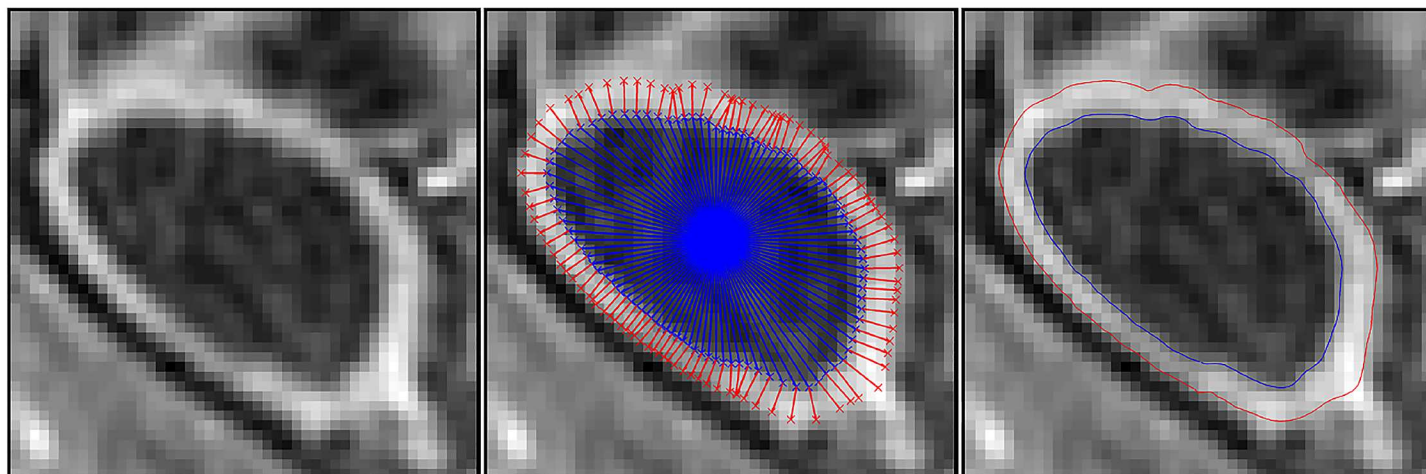
Fig 9. Overview of the wall thickness measurement. A cross-section of the bowel is taken (left), the inner- and outer-walls are detected (centre) and the final contour for both is generated (right).
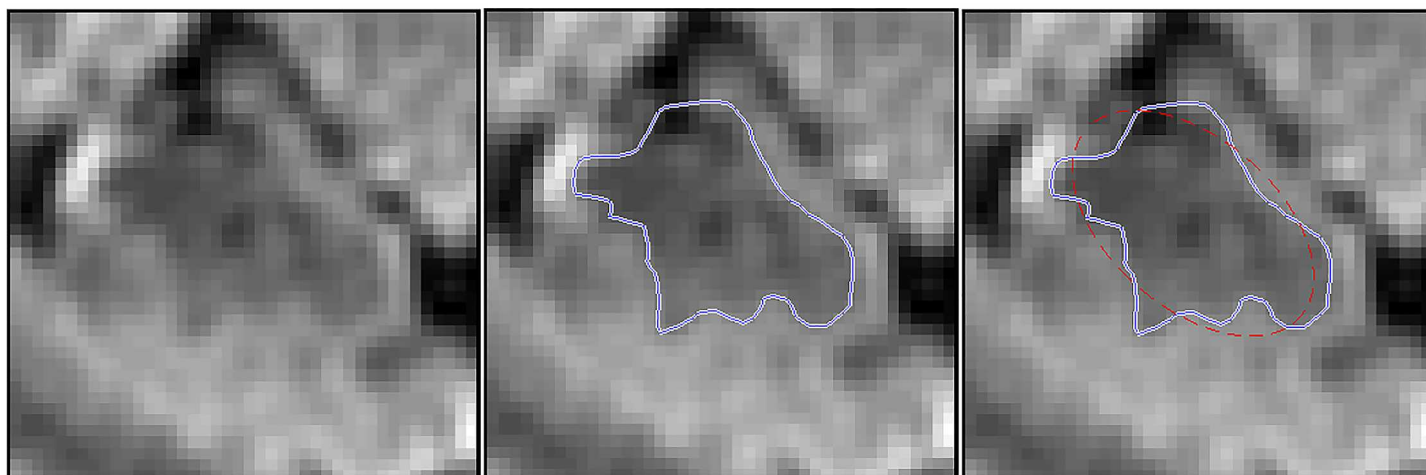
Fig 10. Using the GUI to specify the ellipse parameters for the initial particle filter state. The centre image shows the freehand drawn inner bowel wall contour (solid blue line), and the right image shows the least-square fit ellipse (red dashed line).

2.9 Imaging Protocol

Three hours prior to the scan, participants were requested to drink 3L of 2% mannitol (Baxter, UK) solution to distend the bowel and add contrast. Each patient was cannulated (22G, Introcan Safety, Braun) into the antecubital vein prior to lying in the scanner (3T Philips Achieva, Philips Healthcare, Best, The Netherlands). Each subject was scanned in the prone position with routine anatomical MRI scans acquired following spasmolysis with butyscopolamine (20mg Buscopan, Boehringer Ingelheim).

For this study a 15s breath-hold 3D post-gadolinium contrast (0.1 ml/kg Gadovist 1.0mmol/ml, Bayer Schering Pharma, Berlin, Germany)—T1 high resolution isotropic volume

excitation (THRIVE) sequence was used. Each participant had 90 coronal slices with the following parameters: spatial resolution = $2 \times 2 \times 2mm$, TR = $2.18ms$, TE = $1.02ms$, Averages = 1, acquisition matrix = 228×223, flip angle = 10 degrees using the manufacturer's torso coil.

2.10 Ethics Statement

This research was conducted following approval from the North Hampstead Research Ethics Committee (10/H0720/91, 22/12/2010) and sponsored by University College London Hospitals. Approval, on behalf of the participants, was granted by the Research Ethics Committee to use a limited amount of their anonymised data within UCL Centre for Medical Imaging and selected partner organisation groups for research purposes only.

2.11 Patient Demographics

24 participants with an existing diagnosis of Crohn's disease based on a combination of clinical, biochemical, endoscopic, imaging and histopathological findings were identified (8 male) with the mean age 31.3 years (range 19 to 64).

2.12 Experimental Design

For the purpose of establishing the accuracy of the bowel wall thickness measurement algorithm, 24 patient cases were chosen at random and without exclusion. In each case, between 6 and 8 locations were selected, evenly distributed along the large bowel from rectum to caecum, by arrows pointing in the direction of the inner bowel wall. Two radiologists (AA, GB) independently created a second set of ROIs by measuring the thickness of the bowel wall from a point on the inner bowel wall which has been identified by the study coordinator (AM), such that it is closest to the preselected location (see Fig 11). 4 patient cases were duplicated to allow an estimation of intra-observer error and kept blind to the radiologists. The data was assessed non-consecutively and randomised by the study coordinator, using a pseudorandom number generator. The algorithm described above was executed on each of the cases by selecting a start and end point in the centre of the bowel lumen at $\approx 10cm$ distance along the length of the bowel. To allow for a comparison against the observers' measurements, for each ROI, the thickness measurement where the inner wall position has the smallest Euclidean distance to the observer measurement is selected. If there was no measurement, or the closest measured point was $>5mm$ to the observer ROI, the algorithm is said to have failed to make that measurement.

3 Results

3.1 Overview of results

The results showing the comparison of wall thickness measurements between the algorithm and the individual observer (Fig 12), as well as the level of inter- and intra-observer variability are show in Table 1, and also in the Bland-Altman plots [31] (Fig 13). It can be seen that, in the ROIs which were successfully measured by the algorithm, the mean difference in wall thickness measurement, and the standard deviation of those differences, between the algorithm and the individual observer (mean difference $0.23mm - 0.27mm$, standard deviation $\pm 0.83mm - \pm 0.79mm$) were comparable to that of the intra-observer variability (mean difference $0.16mm$, standard deviation $\pm 0.64mm$). It can also be seen that the distribution of differences of wall thickness measurement is similar, shown in the Bland-Altman plots in Fig 13. However, in around 15% of the ROIs, the algorithm failed to make a measurement within $5mm$ of the same
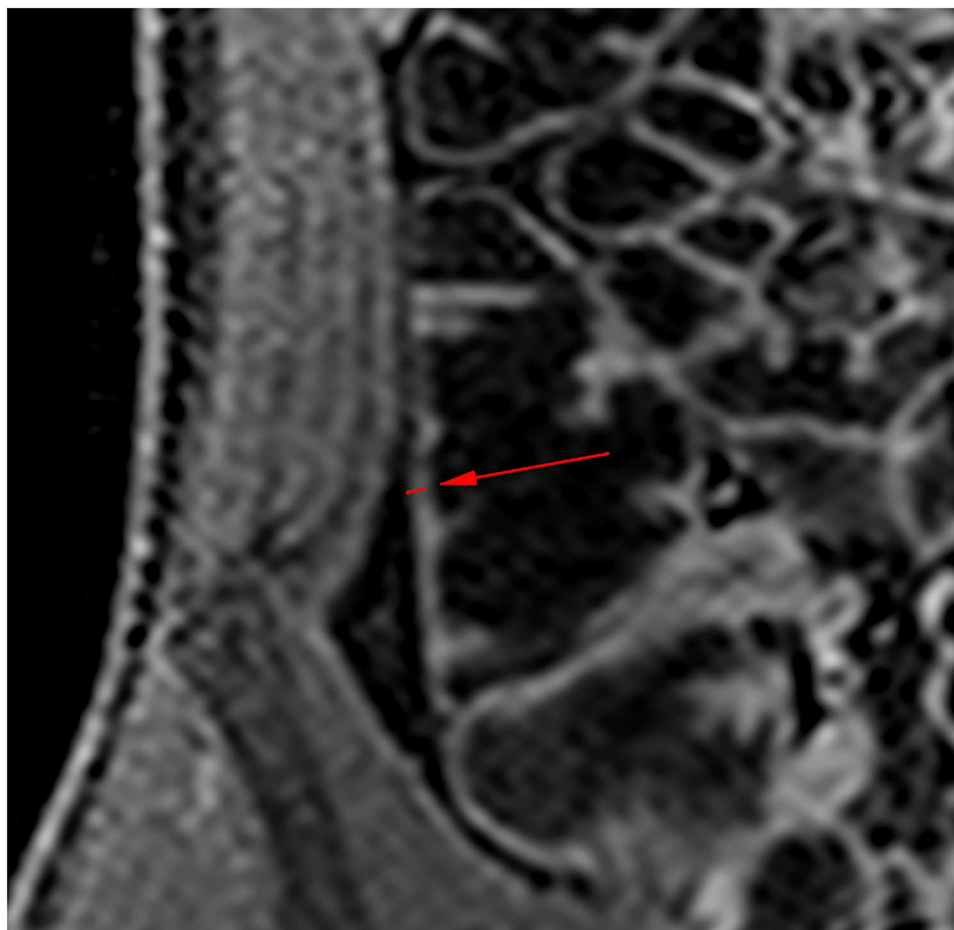
Fig 11. Placements of the ROIs were first selected by the study coordinator, and the approximate position marked with an arrow, pointing towards the bowel wall. The observers independently created a measurement of the bowel wall thickness from an inner bowel wall position that they thought best corresponded with the arrow. This was to minimise the bias on wall thickness measurement induced by the arrow marker.

doi:10.1371/journal.pone.0168317.g011

position as the observer. A section of bowel has been reconstructed from the algorithm measurements and shown in Fig 14.

3.2 Reasons for algorithm failure

When taking the comparison of the magnitude of wall thickness measurements made by the algorithm, and the measurements made by observers 1 and 2, 26 (15.6%) and 24 (14.4%) out of 167 ROIs respectively were not within $5mm$ of each other. In these cases, the primary reasons and the frequency of this occurrence along with examples of regions used in the experiment are listed below:

- Poor wall contrast (4.8%): These areas showed very poor contrast between the lumen and the bowel wall, resulting in the inner and/or outer wall locations being detected incorrectly. This can also make the particle filter tracking fail (see Fig 15).
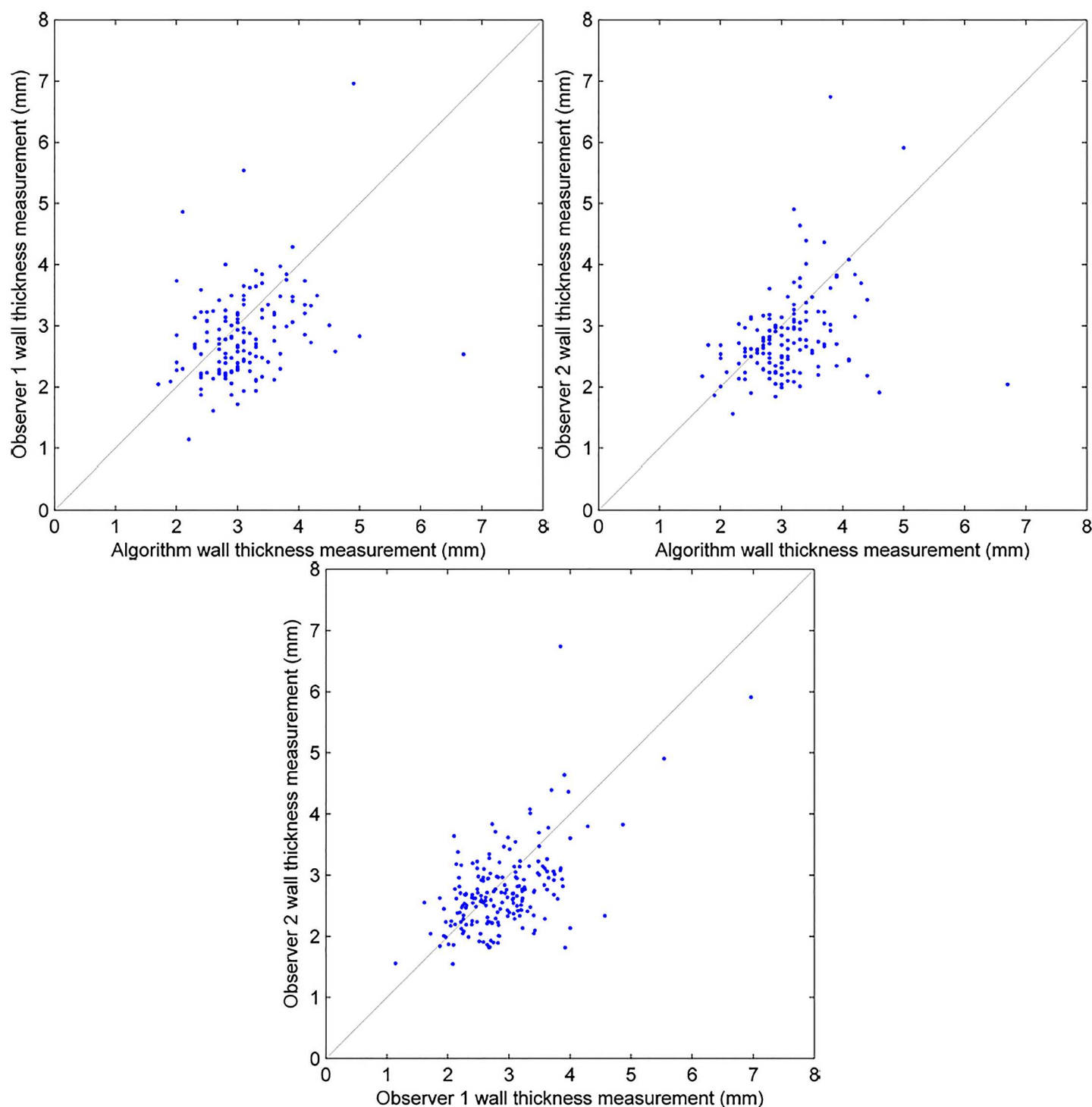
Fig 12. Agreement between the algorithm wall thickness measurements and observer 1 (top left), observer 2 (top right) and a comparison of the individual observer measurements (bottom).

Table 1. Variability and mean difference of wall thickness measurement between the algorithm and the individual observers, the two observers and the observers and their repeat measurements.

	Total ROIs	ROIs included	Mean diff. (mm)	St.D (mm)	95% limits of agreement
Algorithm and observer 1	167	141 (84.4%)	0.23mm	± 0.83mm	± 1.37mm
Algorithm and observer 2	167	143 (85.6%)	0.27mm	± 0.79mm	± 1.30mm
Observer 1 and observer 2	167	167 (100.0%)	0.16mm	± 0.64mm	± 1.05mm
Observer 1 repeat measurements	31	31 (100%)	-0.46mm	± 0.47mm	± 0.77mm
Observer 2 repeat measurements	31	31 (100%)	0.18mm	± 0.43mm	± 0.70mm
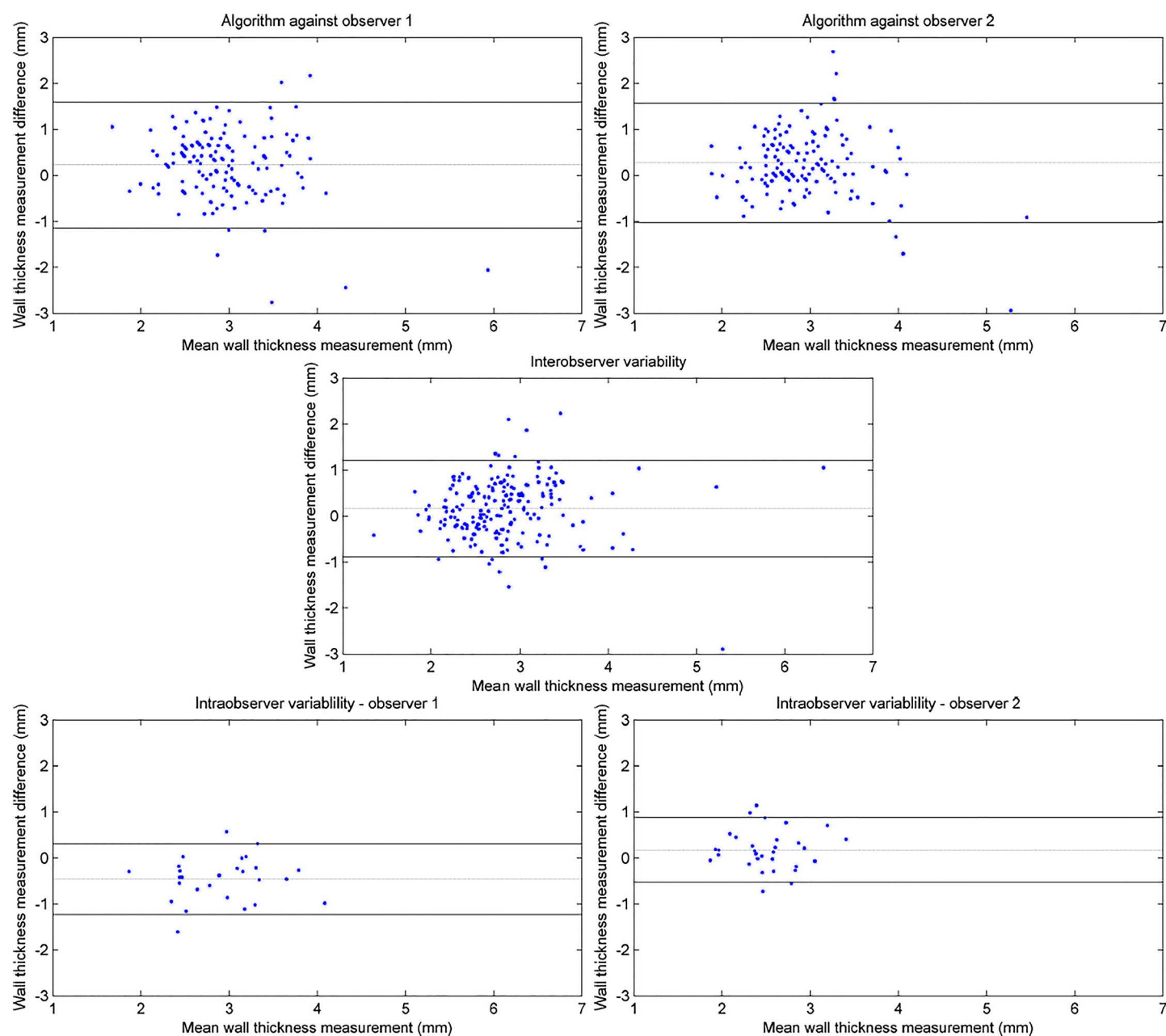
Fig 13. Bland Altman figures showing the variability of wall thickness measurement between: the algorithm and the individual observers (top), the two observers (middle), the observers and their repeat measurements (bottom). The broken line indicates the mean measurement difference. Solid lines indicate the 95% limits of agreement.

Fig 14. A short (80mm) section of stricture in the descending colon of case 22. The inner and outer bowel walls are reconstructed from the points detected by the algorithm.

- Poor preparation (4.2%): Residual faecal matter in the bowel results in areas of high signal which are indistinguishable in terms of intensity value from the bowel wall. Due to the wall detection being made on image gradient values, this residual matter can result in the incorrect detection of the inner bowel wall (see Fig 16).

- Bias field/reconstruction artefact (2.4%): The algorithm is dynamic, updating any threshold values for bowel wall detection as iterations progress along the centreline; however the assumption is made that for each circumferential bowel wall loop, the wall intensity values are relatively constant. In the majority of cases, any inhomogeneities due to the bias field do not hinder the performance of the algorithm, but in a small number of patient cases a steep gradient is observed (see Fig 17).

- Heavily haustrated (2.4%): Problems due to large haustral folds mainly occurred in the caecum. If the detected centreline did not lie exactly central, a given cross section may be intersected by a large haustral fold. As the algorithm searches for the first bowel wall location from the centreline, the haustral fold may be incorrectly identified (see Fig 18).
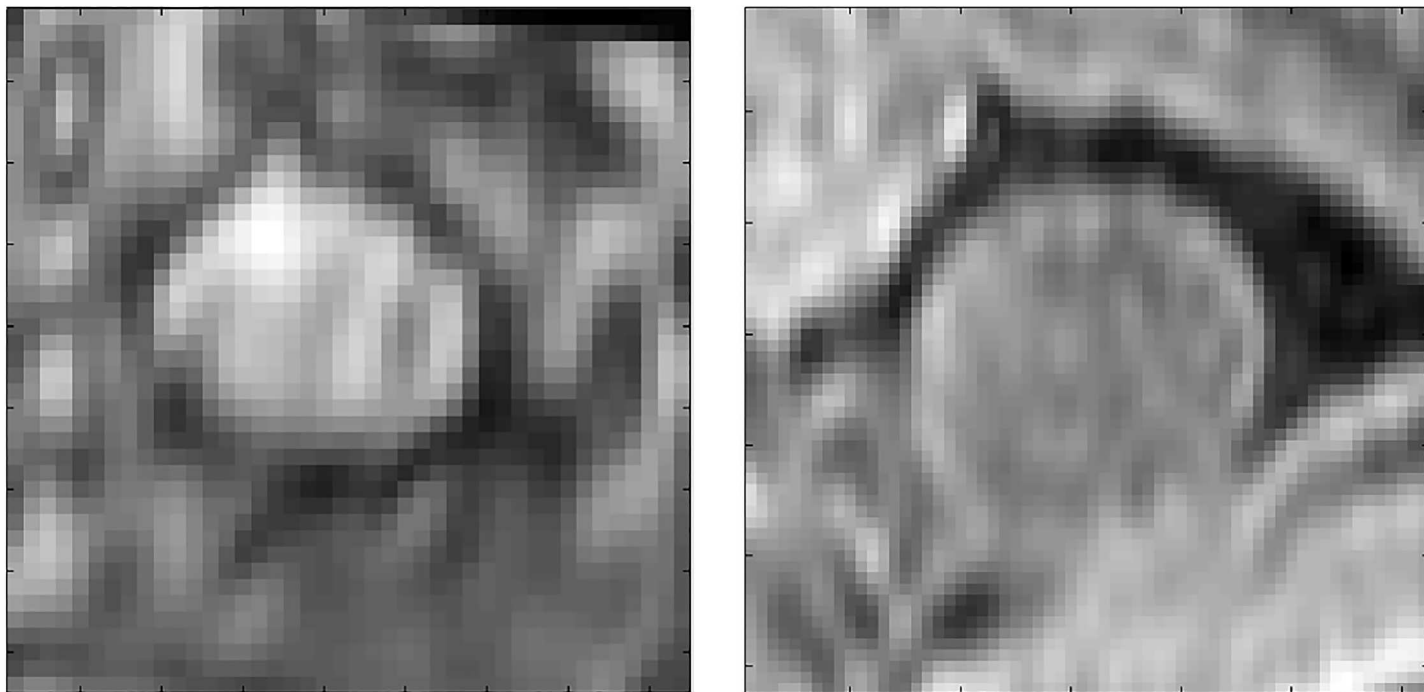
Fig 15. Examples of poor contrast between the lumen and the bowel wall. Each axis 'tick' is 1mm.
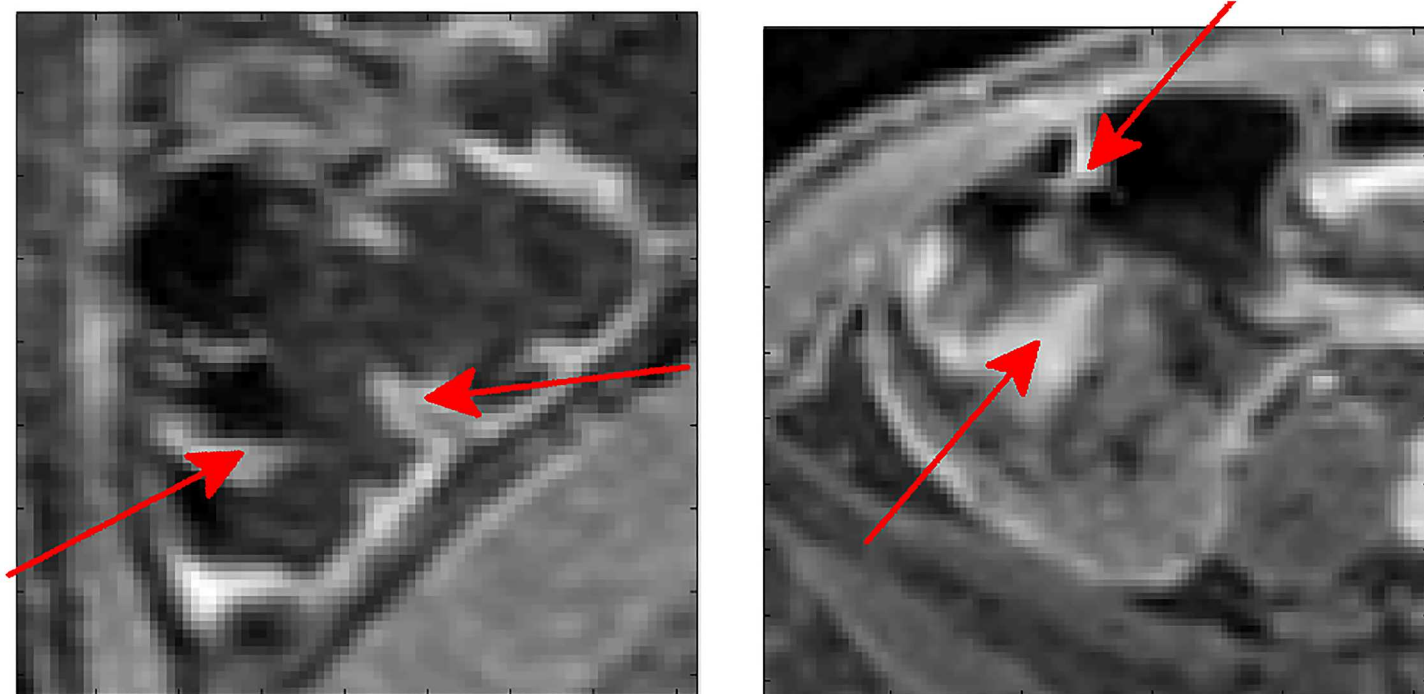
Fig 16. Examples of poorly prepared cases. In both images there is remaining faecal matter which appears as a non homogeneous, high intensity pattern. The image on the left shows an even distribution over the cross section, which makes detecting the bowel wall based on intensity value difficult. The image on the right shows matter (red arrow) floating on the surface of the mannitol solution (image aligned with gravity acting downwards), which may be detected as the location of the bowel wall. Each axis 'tick' is 1mm.
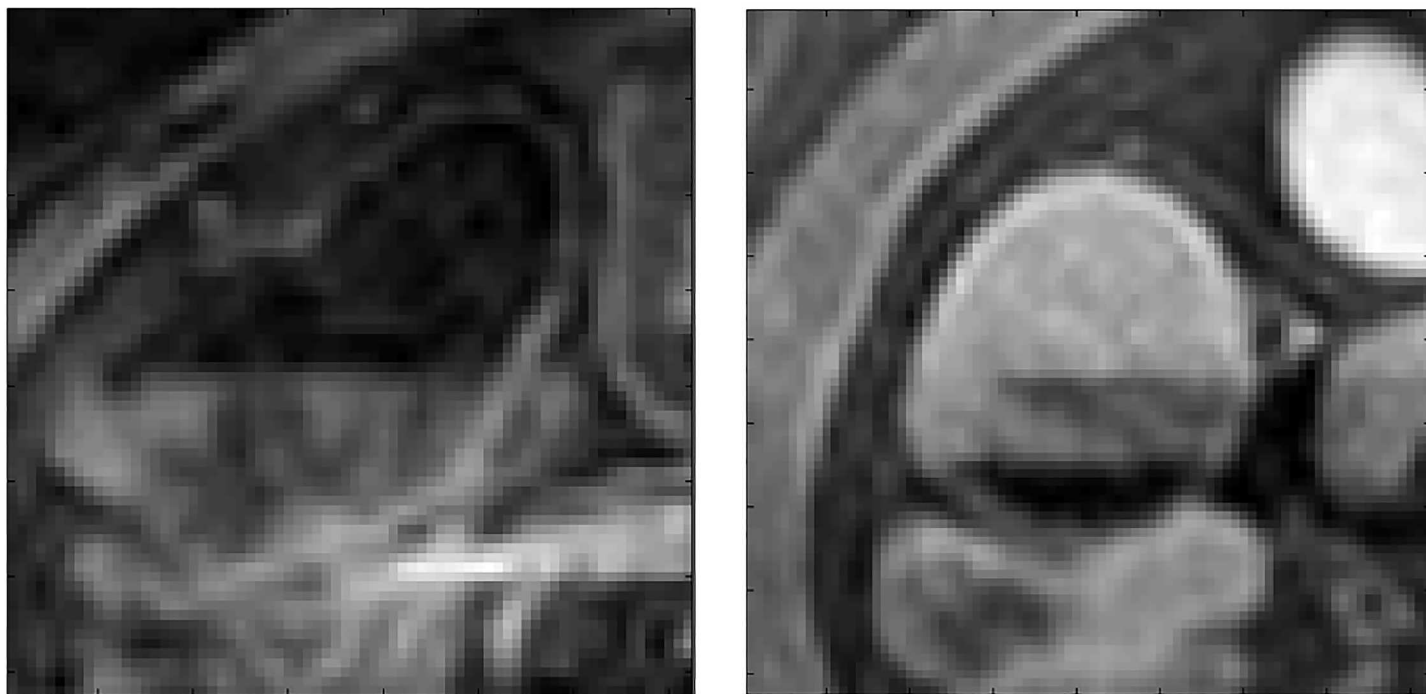
Fig 17. Examples where a strong bias field (left) or reconstruction artefact (right) occurs within a loop of the bowel. As a single intensity value is used for each loop of the bowel wall during the tracking, this strong difference in intensity may result in the incorrect location being detected. Each axis 'tick' is 1mm.
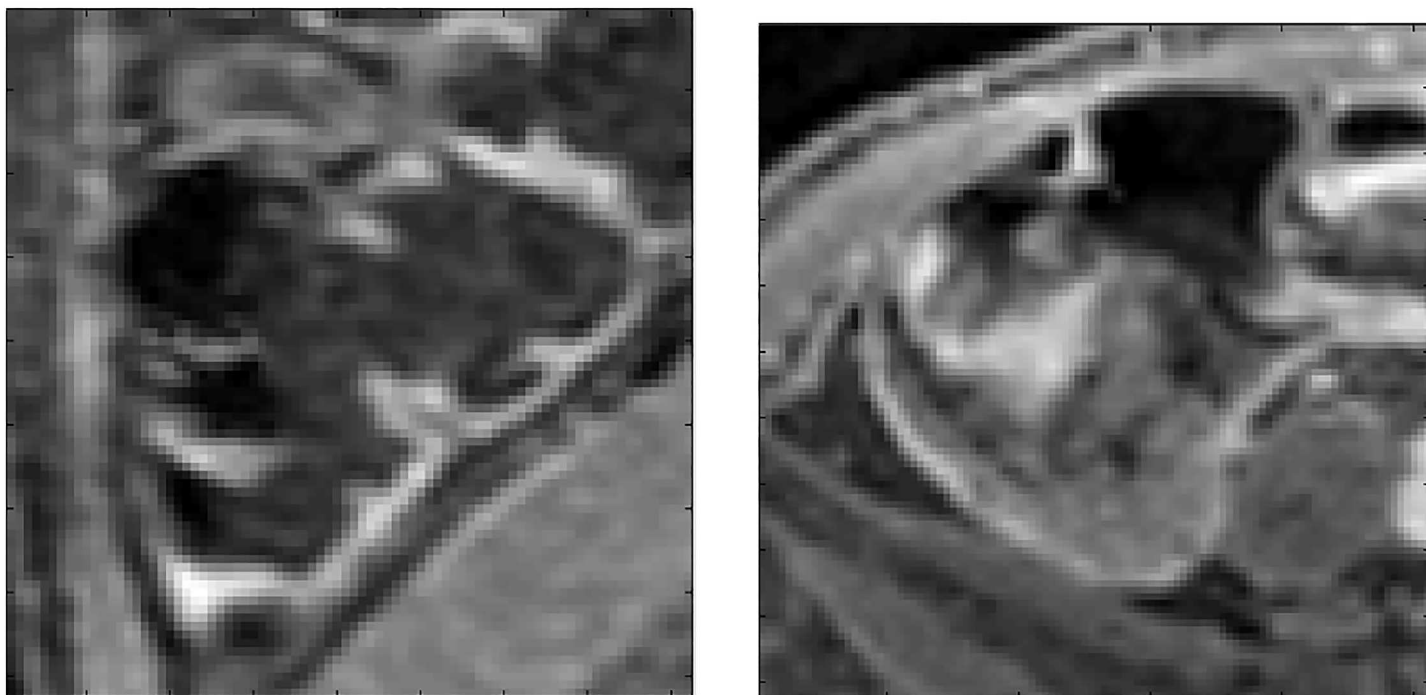
doi:10.1371/journal.pone.0168317.g017

Fig 18. Examples of heavily haustrated regions, indicated by the red arrows, in the descending colon (left) and caecum (right). In these cases more than a single loop of bowel appears in a single cross section, and therefore the incorrect location of the inner bowel wall may be detected. Each axis 'tick' is 1mm.

doi:10.1371/journal.pone.0168317.g018

- Motion artefact (1.2%): In a small number of cases motion artefacts resulted in a blurred image of the bowel wall and therefore the algorithm failed in detecting it correctly.

4 Discussion

The workflow is automated, given a seed point and initial ellipse configuration. Results are promising, showing a similar level of variability between the algorithm and the observer in comparison to the variability between the individual observers; however the algorithm has a slightly lower agreement to the observers. As the method is automated given a manual seed placement, it has the advantage over a human reader that a very large number of wall thickness measurements can be made rather than the relatively small number of manually placed measurements an observer might make. Such information could provide a more accurate mean measurement or allow the reader to compare the variation and distribution of wall thickness. This method also has the potential to make more consistent measurements, something that has been shown to be an issue with the human reader.

However, an obvious disadvantage is the failure of the algorithm in around 15% of cases. This is primarily due to the algorithm's expectation to detect a full loop of bowel in each cross sectional image. Due to the reasons listed above (poor wall contrast, poor preparation, bias field/reconstruction artefact, heavily haustruated sections, motion artefact), this is not possible using the assumptions made in the methods section of this paper, and therefore further domain specific information would have to be incorporated into the algorithm in order to cope with these use cases. Furthermore, the algorithm does not currently give any indication of the accuracy of a given measurement. On many of the cross sectional images it is difficult to give an accurate measurement, even for the human observer and so quantification of measurement accuracy is important to draw any meaningful clinic value from the results. This would be especially important if one wanted to create a mean thickness measurement along a section of bowel, which could be useful in cases of severe inflammation or stricture. To overcome inaccuracies due to poor preparation which occurs frequently in clinical practice, it may be possible to incorporate textural information to better identify lumen and bowel wall. This approach has been used in automatically detecting areas of Crohn's disease in MR volumes [32] by machine learning techniques and could be better used to classify voxel type.

In conclusion, we have presented a method for automated bowel wall thickness measurement which has shown similar levels of variability to two observers in 142 ROIs over 24 patient cases. This is an extremely challenging task as the range of locations picked to assess bowel wall thickness were not representative of clinical cases where optimal regions of good distension are expected. Results using clinically representative data may be better. Further work is needed before clinical use. This should address the reasons for algorithm failure which have been identified to be cases with poor wall contrast, poor preparation, bias field/reconstruction artefact, heavily haustruated sections and motion artefact.

Author Contributions

Conceptualization: TH.

Data curation: AM AJ GB.

Formal analysis: TH AM.

Funding acquisition: DH ST SH SP.

Investigation: AM.

Methodology: TH.

Project administration: AM.

Resources: AM ST.

Software: TH.

Supervision: DH.

Validation: TH AM.

Visualization: TH.

Writing – original draft: TH.

Writing – review & editing: AM DA SH DH ST.

References

1. Dignass A, Van Assche G, Lindsay JO, Lémann M, Söderholm J, Colombel JF, et al. The second European evidence-based Consensus on the diagnosis and management of Crohn's disease: Current management. Journal of Crohn's & colitis. 2010 Feb; 4(1):28–62. Available from: http://www.ncbi.nlm.nih.gov/pubmed/21122489 doi: 10.1016/j.crohns.2009.12.002

2. Kappelman MD, Moore KR, Allen JK, Cook SF. Recent trends in the prevalence of Crohn's disease and ulcerative colitis in a commercially insured US population. Digestive diseases and sciences. 2013 Feb; 58(2):519–25. Available from: http://www.pubmedcentral.nih.gov/articlerender.fcgi?artid=3576554&tool = pmcentrez&rendertype = abstract doi: 10.1007/s10620-012-2371-5 PMID: 22926499

3. Baumgart DC, Sandborn WJ. Crohn's disease. Lancet. 2012 Nov; 380(9853):1590–605. Available from: http://www.ncbi.nlm.nih.gov/pubmed/22914295 doi: 10.1016/S0140-6736(12)60026-9 PMID: 22914295

4. Panes J, Bouhnik Y, Reinisch W, Stoker J, Taylor SA, Baumgart DC, et al. Imaging techniques for assessment of inflammatory bowel disease: joint ECCO and ESGAR evidence-based consensus guidelines. Journal of Crohn's & colitis. 2013 Aug; 7(7):556–85. Available from: http://www.ncbi.nlm.nih.gov/pubmed/23583097 doi: 10.1016/j.crohns.2013.02.020 PMID: 23583097

5. Horsthuis K, Bipat S, Stokkers PCF, Stoker J. Magnetic resonance imaging for evaluation of disease activity in Crohn's disease: a systematic review. European radiology. 2009 Jun; 19(6):1450–60. Available from: http://www.ncbi.nlm.nih.gov/pubmed/19189109 doi: 10.1007/s00330-008-1287-0 PMID: 19189109

6. Punwani S, Rodriguez-Justo M, Bainbridge A, Greenhalgh R, De Vita E, Bloom S, et al. Mural Inflammation in Crohn Disease: Location-Matched Histologic Validation of MR Imaging Features 1. Radiology. 2009; 252(3). Available from: http://pubs.rsna.org/doi/abs/10.1148/radiol.2523082167 doi: 10.1148/radiol.2523082167 PMID: 19635832

7. Taylor SA, Punwani S, Rodriguez-Justo M, Bainbridge A, Greenhalgh R, De Vita E, et al. Mural Crohn disease: correlation of dynamic contrast-enhanced MR imaging findings with angiogenesis and inflammation at histologic examination–pilot study. Radiology. 2009 May; 251(2):369–79. Available from: http://www.ncbi.nlm.nih.gov/pubmed/19276323 doi: 10.1148/radiol.2512081292 PMID: 19276323

8. Rimola J, Ordás I, Rodriguez S, García-Bosch O, Aceituno M, Llach J, et al. Magnetic resonance imaging for evaluation of Crohn's disease: validation of parameters of severity and quantitative index of activity. Inflammatory bowel diseases. 2011 Aug; 17(8):1759–68. Available from: http://www.ncbi.nlm.nih.gov/pubmed/21744431 doi: 10.1002/ibd.21551 PMID: 21744431

9. Steward MJ, Punwani S, Proctor I, Adjei-Gyamfi Y, Chatterjee F, Bloom S, et al. Non-perforating small bowel Crohn's disease assessed by MRI enterography: derivation and histopathological validation of an MR-based activity index. European journal of radiology. 2012 Sep; 81(9):2080–8. Available from: http://www.ncbi.nlm.nih.gov/pubmed/21924572 doi: 10.1016/j.ejrad.2011.07.013 PMID: 21924572

10. Tielbeek JAW, Löwenberg M, Bipat S, Horsthuis K, Ponsioen CY, D'Haens GR, et al. Serial magnetic resonance imaging for monitoring medical therapy effects in Crohn's disease. Inflammatory bowel diseases. 2013 Aug; 19(9):1943–50. Available from: http://www.ncbi.nlm.nih.gov/pubmed/23765176 PMID: 23765176

11. Tielbeek JaW, Vos FM, Stoker J. A computer-assisted model for detection of MRI signs of Crohn's disease activity: future or fiction? Abdominal imaging. 2012 Dec; 37(6):967–73. Available from:

http://www.pubmedcentral.nih.gov/articlerender.fcgi?artid=3517801&tool = pmcentrez&rendertype = abstract doi: 10.1007/s00261-011-9822-x PMID: 22134675

12. Ziech MLW, Bipat S, Roelofs JJTH, Nio CY, Mearadji B, van Doorn S, et al. Retrospective comparison of magnetic resonance imaging features and histopathology in Crohn's disease patients. European journal of radiology. 2011 Dec; 80(3):e299–305. Available from: http://www.ncbi.nlm.nih.gov/pubmed/21295932 doi: 10.1016/j.ejrad.2010.12.075 PMID: 21295932

13. Vos FM, Tielbeek JAW, Naziroglu RE, Li Z, Schueffler P, Mahapatra D, et al. Computational modeling for assessment of IBD: to be or not to be? In: Engineering in Medicine and Biology Society; 2012. p. 3974–3977.

14. Mahapatra D, Schueffler P, Tielbeek JaW, Buhmann JM, Vos FM. A supervised learning approach for Crohn's disease detection using higher-order image statistics and a novel shape asymmetry measure. Journal of digital imaging. 2013 Oct; 26(5):920–31. Available from: http://www.ncbi.nlm.nih.gov/pubmed/23392736 doi: 10.1007/s10278-013-9576-9 PMID: 23392736

15. Mahapatra D, Schüffler P, Tielbeek JAW, Makanyango J, Stoker J, Taylor SA, et al. Automatic Detection and Segmentation of Crohn's Disease Tissues from Abdominal MRI. IEEE transactions on medical imaging. 2013; 32(12):2332–2347. Available from: http://ieeexplore.ieee.org/xpls/abs_all.jsp?arnumber=6600949 doi: 10.1109/TMI.2013.2282124 PMID: 24058021

16. Achanta R, Shaji A, Smith K, Lucchi A, Fua P, Susstrunk S. SLIC superpixels compared to state-of-the-art superpixel methods. IEEE Tranactions on Pattern Analysis and Machine Intelligence. 2012; 34 (11):2274–2281. Available from: http://ieeexplore.ieee.org/xpls/abs_all.jsp?arnumber=6205760 doi: 10.1109/TPAMI.2012.120

17. Mahapatra D, Schüffler P, Tielbeek J, Makanyango J, Stoken J, Taylor S, et al. Active learning based segmentation of crohn's disease using principles of visual saliency. IEEE 11th International Symposium on Biomedical Imaging. 2014; Available from: http://people.inf.ethz.ch/mahapatd/Papers/Conference/Mahapatra_ISBI_2014.pdf

18. Li Z, Caan MWA, Ziech ML, Stoker J, Vliet LJV, Vos FM. 3D Non-rigid Motion Correction of Free-Breathing Abdominal DCE-MRI Data. Abdominal Imaging: computational and Clinical Applications. 2011;p. 44–50.

19. Ashburner J, Friston K. Nonlinear spatial normalization using basis functions. Human brain mapping. 1999; 266:254–266. Available from: http://eecs.vanderbilt.edu/courses/CS359/other_links/papers/1999_Ashburner_Human_Brain_Mapping_spatial_normalization.pdf doi: 10.1002/(SICI)1097-0193(1999)7:4%3C254::AID-HBM4%3E3.0.CO;2-G

20. Nordin N, Rahman N, Myint YM, Aminudin M, Abduljabbar HN, Pahl C, et al. Wall Thickness Measurement of Colon Based on Ultrasound Image Segmentation. 1st WSEAS International Conference on Biomedicine and Health Engineering. 2012;p. 324–329. Available from: http://www.wseas.us/e-library/conferences/2012/Zlin/ENAGROBIO/ENAGROBIO-52.pdf

21. Otsu N. A threshold selection method from gray-level histograms. Automatica. 1979; 20(1):62–66. Available from: http://web-ext.u-aizu.ac.jp/course/bmclass/documents/otsu1979.pdf

22. Arulampalam MS, Maskell S, Gordon N, Clapp T. A tutorial on particle filters for online nonlinear/non-Gaussian Bayesian tracking. IEEE Transactions on Signal Processing. 2002; 50(2):174–188. Available from: http://ieeexplore.ieee.org/lpdocs/epic03/wrapper.htm?arnumber=978374 doi: 10.1109/78.978374

23. Shim H, Kwon D, Yun ID, Lee SU. Robust segmentation of cerebral arterial segments by a sequential Monte Carlo method: particle filtering. Computer methods and programs in biomedicine. 2006 Dec; 84 (2-3):135–45. Available from: http://www.ncbi.nlm.nih.gov/pubmed/17045696 doi: 10.1016/j.cmpb.2006.09.001 PMID: 17045696

24. Wang W, Jüttler B, Zheng D, Liu Y. Computation of rotation minimizing frames. ACM Transactions on Graphics. 2008 Mar; 27(1):1–18. Available from: http://portal.acm.org/citation.cfm?doid=1330511.1330513 doi: 10.1145/1409060.1409071

25. Bergman N. Recursive Bayesian estimation: Navigation and tracking applications; 1999. Available from: http://www.student.nada.kth.se/kurser/kth/2D5342/kurspaket/NiclasBergman.pdf

26. Yang C, Duraiswami R, Gumerov NA, Davis L. Improved fast gauss transform and efficient kernel density estimation. Proceedings Ninth IEEE International Conference on Computer Vision. 2003;p. 664–671 vol.1. Available from: http://ieeexplore.ieee.org/lpdocs/epic03/wrapper.htm?arnumber=1238383

27. Adalsteinsson D, Sethian JA. A Fast Level Set Method for Propagating Interfaces. Journal of computational physics. 1994; 118(2):269–277. doi: 10.1006/jcph.1995.1098

28. Wang W, Joe B. Robust computation of the rotation minimizing frame for sweep surface modeling. Computer-Aided Design. 1997; 29(5):379—391. doi: 10.1016/S0010-4485(96)00077-2

29. Weiss Y, Freeman WT. On the optimality of solutions of the max-product belief-propagation algorithm in arbitrary graphs. IEEE Transactions on Information Theory. 2001; 47(2):736–744. Available from: http://ieeexplore.ieee.org/lpdocs/epic03/wrapper.htm?arnumber=910585 doi: 10.1109/18.910585

30. Gander W, Golub GH, Strebel R. Least-squares fitting of circles and ellipses. BIT Numberical Mathematics. 1994 Dec; 34(4):558–578. Available from: http://link.springer.com/10.1007/BF01934268 doi: 10.1007/BF01934268

31. Bland JM, Altman DG. Agreement between methods of measurement with multiple observations per individual. Journal of biopharmaceutical statistics. 2007 Jan; 17(4):571–82. Available from: http://www.ncbi.nlm.nih.gov/pubmed/17613642 doi: 10.1080/10543400701329422 PMID: 17613642

32. Mahapatra D, Schueffler P, Tielbeek JAW, Buhmann JM, Vos FM. A supervised learning based approach to detect crohn's disease in abdominal MR volumes. Abdominal Imaging Computational and Clinical Applications. 2012;p. 97–106. Available from: http://link.springer.com/chapter/10.1007/978-3-642-33612-6_11